

Oceanographic Measurements

This chapter describes various methods to measure the oceanographic variables that are dynamically significant. After a brief overview of the various motions and their temporal and spatial scales, the challenges of making measurements in a vast, inhospitable, and unforgiving environment are described. Then point measurements (pressure, temperature, salinity, sound speed, density, and velocity), Lagrangian measurements (floats and dye dispersion), and remote sensing methods (acoustic and electromagnetic) are described. Because many of the practical problems of oceanographic measurements are associated with the complete measurement system, examples of these and illustrative case studies of several experiments are given.

18.1 Oceanography	1179
18.1.1 Oceanographic Processes.....	1179
18.1.2 Challenges of the Environment.....	1181
18.2 Point Measurements	1182
18.2.1 Pressure.....	1182
18.2.2 Temperature.....	1182
18.2.3 Salinity.....	1183
18.2.4 Sound Speed	1185
18.2.5 Density	1185
18.2.6 Velocity.....	1186
18.3 Lagrangian Techniques	1188
18.3.1 Surface Drifters	1188

18.3.2 Deep Ocean Floats	1189
18.3.3 Dispersion	1190
18.4 Remote Sensing	1192
18.4.1 Acoustic Doppler Current Profilers (ADCP)	1192
18.4.2 Acoustic Tomography	1195
18.4.3 Acoustic Correlation Techniques	1199
18.4.4 Electromagnetic Sensing Using the Geomagnetic Field	1199
18.4.5 Surface Current Mapping Using Radar Backscatter	1201
18.4.6 Satellites	1202
18.5 Measurement Systems	1203
18.5.1 Expendable Sensors.....	1203
18.5.2 HPIES	1203
18.5.3 Moored Profiler.....	1204
18.5.4 TriSoarus Towed Vehicle	1204
18.5.5 Turbulence and Small-Scale Structure	1205
18.5.6 Floats	1205
18.5.7 Gliders	1207
18.5.8 Autonomous Undersea Vehicles (AUVs)	1207
18.5.9 LEO-15	1207
18.6 Experiment Case Studies	1208
18.6.1 Hawaii Ocean Mixing Experiment (HOME)	1209
18.6.2 Fluxes, Air–Sea Interaction, and Remote Sensing (FAIRS).....	1212
References	1214

18.1 Oceanography

The oceans cover 70% of the Earth and profoundly affect the planet and our lives. The ocean is the flywheel of the climate, and if we hope to predict climate change, we must intimately understand the processes within and bounding the ocean, from the smallest scales of turbulent mixing to the largest scales of global ocean circulation (Fig. 18.1). The majority of the world's population lives nearby the sea and is directly affected by the marine weather, coastal ocean ecosys-

tems, and associated hazards such as storm surges and tsunamis. Ocean ecosystems and the *environmental services* they provide, from food to carbon sequestration, are directly affected by ocean dynamics over the full range of scales. As governments and citizens increasingly appreciate the importance of knowing the present and future states of the ocean, more effort is being placed on measuring, observing, and understanding the ocean.

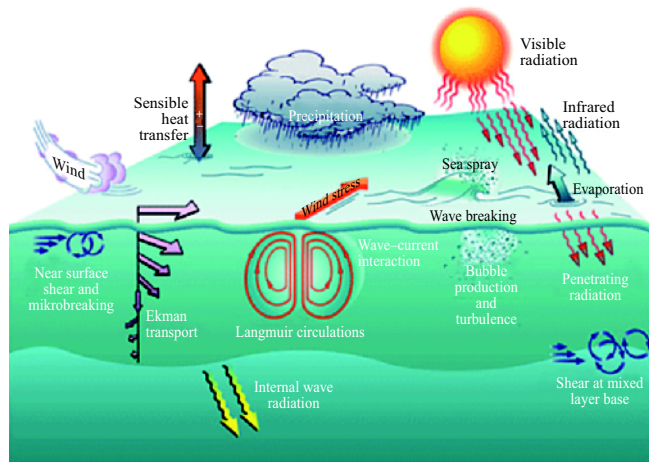


Fig. 18.1 Some of the many physical processes occurring in the ocean (courtesy of J. Doucette, Woods Hole Oceanographic Institution)

18.1.1 Oceanographic Processes

Ocean processes are active over a multitude of time and space scales (Fig. 18.2). Most are affected by the two major distinguishing characteristics of ocean flow: stratification and the Earth's rotation. Stratification can inhibit turbulence and, because it is determined both by temper-

ature and salinity, double diffusion can occur. Rotation causes the Ekman spiral, the turning of the current vector with depth given a surface wind stress. The combination of the stratification and rotation is responsible for internal waves, ranging from nearly horizontal motions just above the inertial frequency to nearly vertical motions close to the buoyancy frequency. Planetary waves arise from the change in Coriolis force with latitude; examples are eastward-propagating equatorial Kelvin waves and westward-propagating Rossby waves.

Ocean flow is almost geostrophic, i.e., the Coriolis force almost balances the horizontal pressure gradient force. The kinematic geostrophic equations relating the horizontal velocity components u and v to the pressure gradient are:

$$u = - \left(\frac{1}{f\rho} \right) \left(\frac{\partial p}{\partial y} \right) \quad \text{and} \\ v = \left(\frac{1}{f\rho} \right) \left(\frac{\partial p}{\partial x} \right), \quad (18.1)$$

where ρ is density and f is the Coriolis parameter ($2\Omega \sin \varphi$, where Ω is the Earth's angular velocity and φ is the latitude). These equations do not include dynamics. Much of the interesting fluid mechanics is in the *residual* ageostrophic, time-dependent flow. While often (but not necessarily) small, the latter have profound effects on the flow.

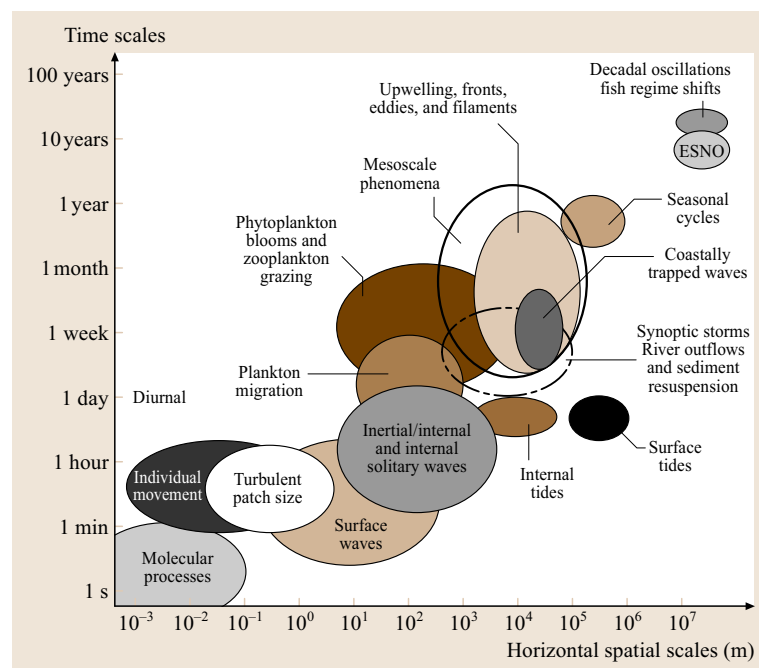


Fig. 18.2 Time and space scales of oceanic processes

Two major challenges confront the oceanographer making measurements: the limitations of the instrumentation, and the difficulty in obtaining adequate spatial and temporal sampling. This chapter primarily addresses the first, but it is necessary to note that sampling errors are the largest source of errors in oceanography. As one wise oceanographer has noted, the first century of modern oceanography was one of undersampling [18.1]. Another states: “The absence of evidence was taken as evidence of absence”. The great difficulty of observing the ocean meant that when a phenomenon was not observed, it was assumed it was not present. The more one is able to observe the ocean, the more complexity and subtlety appears [18.2].

When planning, executing, and analyzing the results of an experiment, it is crucial to find means to overcome the problems of undersampling.

18.1.2 Challenges of the Environment

The dynamic air-sea interface, high pressures at depth, corrosion, and biofouling are just some of the challenges of making ocean measurements that face the experimental fluid mechanist. Much ocean work is still done from ships at the mercy of the weather; no matter how good the ship, operations are sometimes impossible. In fair weather, the ship is always moving, complicating the deployment and recovery of equipment. Making measurements on either side of the air-sea interface is faced with problems of spray, salt deposition, dynamic loading, mechanical fatigue, marine growth, and biofouling of sensors.

The combination of high pressures at depth and saltwater corrosion is challenging to overcome. The high pressures encountered deploying instrumentation at any significant depth dictate the geometry of instrument housings, which are typically either spheres or cylinders. Spheres are the *ideal* shape, if they can be made easily. Cylinders are often more convenient to fit circuit boards and to maintain. Squat-aspect-ratio cylinders with internal bracing are used occasionally for large internal components (such as commercial ethernet routers).

To minimize or reduce corrosion requires proper selection of materials. If possible, instrument housings and platforms must be made of materials that are either inherently noncorrosive (e.g., glass, plastics, titanium) or are protected against corrosion. Glass has been used for decades and, if used appropriately, is robust and inexpensive, even to full ocean depth; the 375 mm-diameter, 25 mm-wall-thickness glass sphere is a well-proven instrument housing. Various plastics are adequate for

shallow depths less than 600 m. If metal housings are used, attention must be paid to the galvanic properties and galvanic connections with other metals; if current flows, the case will corrode and eventually fail. However, if one accepts a ≈ 0.2 mm/y loss of material, mild steel can be used. Carbon fiber housings are starting to be used for large pressure cases (e.g., for cameras) or for deep use requiring specific geometrical shapes (e.g., gliders). An extreme environment for instrument materials is deep hot vents with effluent temperature $> 350^\circ\text{C}$, pH ≈ 2 , and precipitating chemicals.

O-rings are typically used to seal the endcaps of pressure cases or through-case penetrators/connectors; however, if a lifetime longer than 10 years is required, materials such as polyethylene should be considered. A note of caution: O-rings and connectors are the number one reason for instrument failure.

Yet another major problem is biofouling. In the shallow-water photic zone, marine life can grow very rapidly and completely cover an instrument; at depth, bacterial films (and eventually mats) are pervasive. There are no panaceas for this problem; some remedies include special paints and chemicals (already severely regulated in 2005), copper shutters, use of heat, ultraviolet light (e.g., a useful byproduct of some camera lights), conductive coatings on optical surfaces, and special coatings developed for biomedical use that resist biologically active molecules.

The absence of easily available power and communications severely hamper *in situ* measurements. Often instruments must use less than one watt of power (often milliwatts) and a preset sampling schedule. Fortunately, the electronics and data storage part of an instrument are becoming more efficient so the challenge is more in making the actual sensor/transducer more efficient. In an effort to remove the power and communication restriction, various national and international programs are being initiated with the goal of providing power and communications infrastructure. This will be accomplished with sea-floor cable systems with nodes (up to 10 kW and 1 Gb/s), or with deep-sea buoys with power and communication capability being supplied to the seafloor for surrounding sensor networks. Satellites are now providing accurate navigation [e.g., the global positioning system ([GPS](#))] and modest communications (Iridium). Newer and better batteries, solar cells, fuel cells, and *in situ* power generation may provide solutions.

The greatest challenge is perhaps associated with cost and logistics. Day rates for US academic ships range from \$10 000 for a 40 m coastal ship to \$40 000

for an 85 m global-class ship with a remotely operated vehicle. These ships are relatively slow (12 kt) so transit times to remote locations and associated cost can be high. Ocean observing satellite costs are much higher, though usually the user does not

pay the full cost. New paradigms centered on sustained long-term presence (e.g., cabled systems) will have their own logistical and cost challenges. These problems often outweigh those associated with actual measurements.

18.2 Point Measurements

Fundamental oceanographic point measurements are pressure, temperature, salinity, and sound speed; density is usually calculated as an empirical function of these (usually the first three). Pressure, density, and velocity are state variables in the dynamical equations. Various sensors used to make point measurements are described here. It may be useful for the reader to compare this section with Sect. 17.1, which discusses point measurements in the atmosphere.

18.2.1 Pressure

Pressure is a fundamental, and fortunately, routine measurement in oceanography. The SI unit of pressure is the pascal (Pa , 1 N/m^2); often the unit decibar is used because 1 dbar (10^4 Pa) is very nearly equivalent to the hydrostatic pressure of 1 m of water.

The measurement of pressure is used primarily for two purposes: for inferring depth and as a vertical coordinate for other measurements, and for use in the dynamical context. A strain gage is the simplest and least-expensive instrument for measuring pressure; accuracy is about $\pm 1\%$ of full scale.

A typical precision pressure transducer used for full-ocean-depth work is shown in Fig. 18.3. This transducer

uses a very thin quartz crystal beam, electrically induced to vibrate at its lowest resonant mode. The oscillator is attached to a Bourdon tube that is open at one end to the ocean environment. As the pressure increases the Bourdon tube uncurls, stretching the quartz crystal and increasing the vibrational frequency. Conversely, a reduction in pressure causes the Bourdon tube to curl more tightly, thereby compressing the quartz crystal and lowering the vibrational frequency. These quartz frequency changes can be measured very precisely and the frequency changes are then converted into the corresponding changes in pressure. A small temperature dependence is accounted for using an independent thermistor. The sensor response is inherently rapid, and is limited in practice to how precise a measurement is desired and the frequency measurement method; they are often used in profiling systems (described below) sampling at 24 Hz. To measure pressure on the seafloor in the open ocean for the purpose of tsunami detection, averaging times greater than a minute or so are required. In this case, the transducer is sensitive to changes in pressure of less than one millimeter of water [18.3]. Long-term drift can be minimized and characterized by aging the device at high pressure for several months in the laboratory.

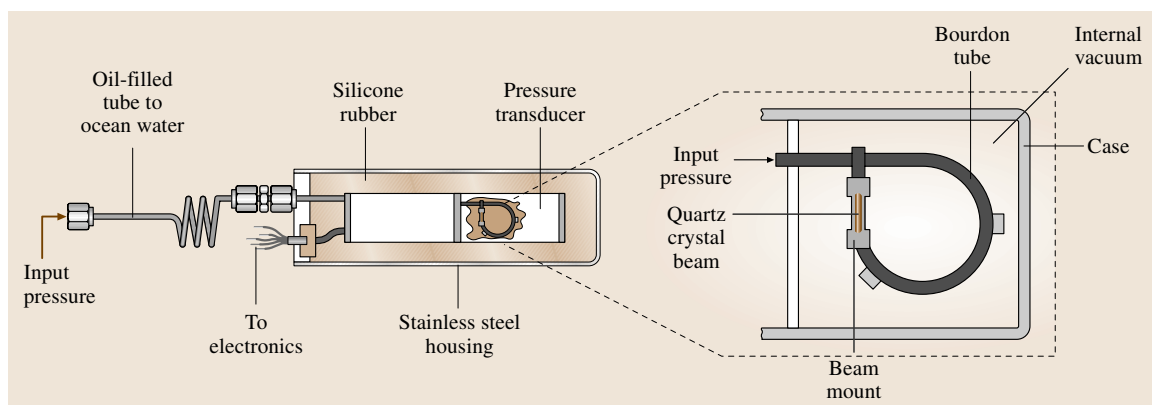


Fig. 18.3 Quartz pressure transducer (Paroscientific, Redmond)

18.2.2 Temperature

Temperature is now routinely measured with a high degree of accuracy using thermistors. One such temperature sensor consists of a glass-coated thermistor bead that is pressure-protected inside a 0.8 mm-diameter thin-walled stainless-steel tube (Sea-Bird Electronics, Bellevue). Exponentially related to temperature, the thermistor resistance is the controlling element in an optimized Wien bridge oscillator circuit. The resulting sensor frequency is inversely proportional to the square root of the thermistor resistance, and is in the range 2–6 kHz, corresponding to temperatures of -5°C to $+35^{\circ}\text{C}$. These sensors have a drift of less than 0.001°C per six-month period and the time response is $\pm 0.010\text{--}0.065$ s. Careful calibration procedures yield an overall transfer accuracy against a platinum reference thermometer within 0.0002°C .

18.2.3 Salinity

Salinity is a measure of the quantity of dissolved salts in ocean water. Seawater is a complex mixture of many ions with 11 major constituents making up more than 99.99% of all dissolved materials. These constituents are very well mixed through the world's oceans and are found in nearly constant proportions. This means that, although the salinity may vary from place to place, the major constituents are present in the same relative proportions. Salinity is now measured as practical salinity units (psu). The United Nations Educational, Scientific, and Cultural Organization (UNESCO) practical salinity scale of 1978 (PSS78) defines salinity in terms of an electrical conductivity ratio (relative to *standard* seawater), and so is dimensionless. Nominally, a salinity of 35 psu means that 35 kg of salt is dissolved per 1000 kg of seawater. Open-ocean salinities are generally 32–37 psu.

Conductivity (reciprocal resistivity) is an intrinsic property of seawater from which salinity and density

may be derived. As conductivity is a strong function of temperature, effects due to the latter must be accounted for.

Oceanographic sensors cannot measure conductivity directly; instead they measure conductance, i.e., the voltage produced in response to the flow of a known electrical current. Conductivity is calculated from the conductance measured by the sensor using a scale factor or cell constant that depends on the ratio of length and cross-sectional area of the sampled water volume in which the electrical current actually flows. In certain types of cells, the length-to-area ratio corresponds very closely to the physical dimensions of the cell. However, in most cases, the sample volume cannot be directly measured to the necessary accuracy.

The determination of conductivity derives from:

$$R = \rho \frac{L}{A}, \quad (18.2)$$

where R is the resistance (1/conductance), ρ is the resistivity (1/conductivity), L is the length of sampled water volume, and A is the cross-sectional area of the sampled water volume. Note the equal importance of sample geometry and measured resistance in the determination of conductivity. (Conductance has units of siemens (S), equivalent to reciprocal ohms or volts/ampere. Conductivity has units of S/m.)

There are three main engineering problems: how to make an electrical connection to the water (difficult but not limiting), how to measure the resistance of the water to which the connection has been made (not difficult), and how to maintain a stable cell geometry (the limiting problem). The first problem is addressed by using electrodes or transformer coupling (inductive). In the latter case, one transform core is used to couple to the water, and the second measures the induced current. For the former, the electrodes must be stable and low resistance (e.g., platinum). The second problem is easily solved with reasonable resistance measuring circuits. The last

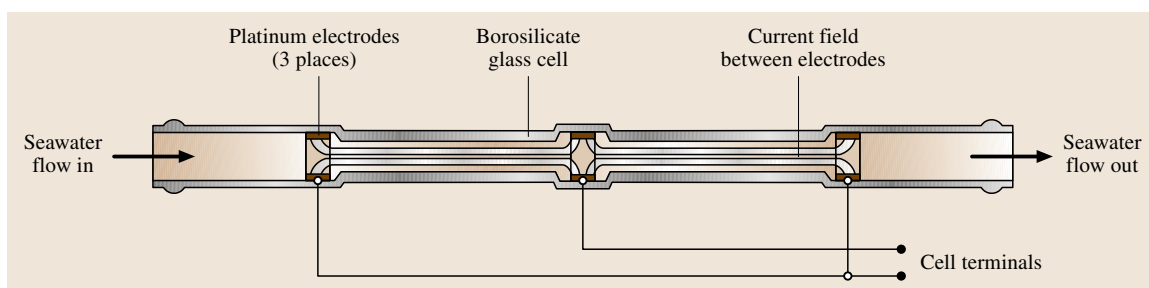


Fig. 18.4 A three-electrode conductivity cell (Sea-Bird Electronics, Bellevue)

problem, though, requires stable geometry of the sensing electric field.

In some sensors, the electric field is contained entirely within the geometry of the cell; in others, the field extends out into the free field and can be affected by nearby objects (e.g., the instrument case).

For field work the three-electrode conductivity cell has its sensing electric field entirely within the cell (Fig. 18.4). Because of its geometry (4 mm internal diameter) seawater must be pumped through it; combined with a temperature sensor in the same fluid circuit and a fixed-flow-rate pump, the sensor and flow time constants are well known and the density can be accurately calculated without any *spiking*. Slowly leaching anti-foulant chemicals can easily be inserted into the fluid circuit to prevent any biological growth and attendant geometry changes. The measurement range is 0.0–7.0 S/m, the initial accuracy is 0.0003 S/m, the stability is 0.0003 S/m per month, and the resolution is 0.00004 S/m at 24 Hz.

A typical inductive cell is a simple open cylinder with two transformer windings around it. The electric field extends outside the cylinder significantly. An alternating voltage in the audio frequency range is applied to one transformer. This induces a voltage in the seawater circuit. The resulting current is directly proportional to the conductivity of the seawater and is measured by the second transformer. To overcome the often ill-defined geometry of such a cell, a new sensor has been developed (Fig. 18.5). It consists of two ceramic tubes mounted parallel to each other. The ends of each tube are fixed to ceramic boxes. Each tube has a pair of toroidal transformers fitted coaxially over them. The two cores act as charge pumps pulling the current lines from one end reservoir down the opposite tube. This situation is

very similar in operation to guard electrodes used on the open ends of a tube electrode sensor. Because the cells are large and freely flushing, pumping is not required. Because the electric field is internal to the sensor (thus the name, nonexternal inductive conductivity sensor (NXIC)), anti-foulant chemical can be placed around the ends of the sensor.

To calibrate conductivity cells in situ to obtain the best possible salinity accuracy (currently $\approx \pm 0.002$ psu), water samples are collected and then compared with International Association for the Physical Sciences of the Oceans (IAPSO) standard seawater in the laboratory. An accepted commercial standard for in-laboratory measurement of water samples is the Guideline Instruments, Ltd. *Autosal*. The main feature of this instrument is a four-electrode conductivity cell immersed in a high-precision temperature-controlled water bath that allows a sequential measurement of standards and samples. Standard seawater is required to calibrate the instrument at regular intervals. The electric field is contained entirely within the cell and is therefore not affected by external factors.

A new, smaller and more-portable unit has been developed recently [18.4]. A dual inductive cell system removes the need for a highly stable bath temperature and gives direct reading of the conductivity ratio of the sample against standard seawater. A single master oscillator is used to drive the coil which transects both of the sample-containing rings of fluid, inducing the same proportion of flux in both measuring cells. Each ring has an independent pick-up coil, and the signals from these give the raw outputs. The dual cell removes the need for highly stable bath temperatures, and the cells are surrounded by a well-stirred oil bath to ensure thermal uniformity. Every sample is standard-

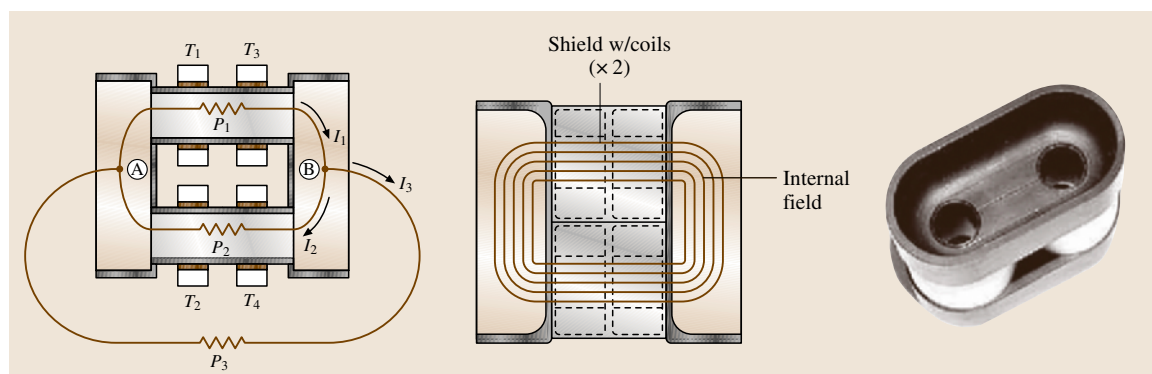


Fig. 18.5 Schematic, sensor, and internal field lines of the NXIC inductive conductivity sensor (Falmouth Scientific, Cataumet)

ized, and the standard itself is enclosed in glass to preserve the integrity of the reference measurement for weeks (and reduces cost). The instrument complements laboratory salinometers; it was developed as a collaboration between RBR Ltd., Guideline, and the Marine Hydrophysical Institute, Ukraine.

18.2.4 Sound Speed

The speed of sound in seawater is a strong function of temperature and pressure and a weak function of salinity. In some cases it is easier or more economical to measure temperature, pressure, and the speed of sound to then determine salinity. In other cases the speed of sound is desired directly or to infer temperature. In the acoustic measurement of water velocity, the speed of sound often enters into the equations.

A simple equation for the speed of sound in seawater is that of Mackenzie:

$$\begin{aligned} C(T, S, D) = & 1448.96 + 4.591T - 5.304 \times 10^{-2}T^2 \\ & + 2.374 \times 10^{-4}T^3 + 1.340(S - 35) \\ & + 1.630 \times 10^{-2}D + 1.675 \times 10^{-7}D^2 \\ & - 1.025 \times 10^{-2}T(S - 35) \\ & - 7.139 \times 10^{-13}TD^3, \end{aligned} \quad (18.3)$$

where T is temperature in degrees Celsius, S is salinity in psu, D is depth in meters; the range of validity is temperature 2–30 °C, salinity 25–40 psu, and depth 0–8000 m [18.5].

If this is linearized one obtains

$$\delta C = 4.598T + 1.348S + 0.0163\delta D, \quad (18.4)$$

where δ represents a small perturbation. The nominal sound speed in the ocean is 1500 m/s. For a typical ocean temperature change of 1 °C, the sound speed changes roughly 4 m/s; for a 1 psu change, the change in sound speed is roughly 1 m/s; for every 1000 m increase in water depth, the sound speed increases by 16 m/s. Typical salinity changes in the ocean are much smaller than 1 psu and in many underwater acoustics applications the effects of salinity can be ignored. For precise work, one should reference the UNESCO standard equation [18.6].

For *point* measurements of sound speed, time-of-flight sound velocimeters have a specified accuracy of ± 0.05 m/s, with a response time of ≈ 0.1 ms and a path length of 10–30 cm (Applied Microsystems, Ltd.). It is shown below that elements of acoustic tomography are in essence large sound velocimeters.

Acoustics plays a significant role in oceanographic measurements as will become evident below. A recent

text presents the fundamentals of acoustical oceanography including studies of the near-surface ocean, bioacoustics, ocean dynamics, and the ocean bottom [18.7].

18.2.5 Density

Density is an empirical function of temperature, salinity, and pressure. Because much of the ocean circulation is governed by small density differences, density is a crucial measurement and attention must always be paid to precision and accuracy. Seawater density changes from roughly 1028 kg/m³ at the surface to 1054 kg/m³ at a depth of 6000 m. At the sea surface temperature ranges from -1.8 °C to ≈ 32 °C with corresponding densities of 1028 kg/m³ and 1021 kg/m³. While extremes of salinity are ≈ 34 psu to 37 psu, most ocean water is in the range 34.6–34.8 psu with a corresponding change in density of ≈ 0.17 kg/m³.

Because salinity is difficult to measure directly in situ, electrical conductivity, sensitive to temperature and salinity, is measured instead; an independent measurement of temperature is relatively easy, permitting the salinity signal to be extracted. Density is commonly measured using a conductivity–temperature–

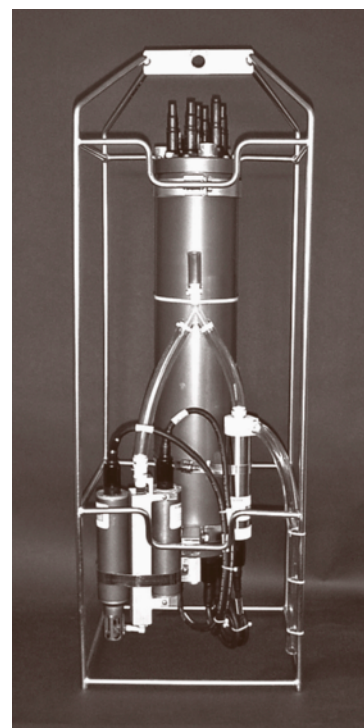


Fig. 18.6
Profiling conductivity–temperature–density (CTD) unit with pressure and pumped temperature, conductivity, and dissolved oxygen sensors (Sea-Bird Electronics, Bellevue)

depth/pressure (**CTD**) sensor package; an example is shown in (Fig. 18.6). This one is deployed on an electrical–mechanical wire from a ship in a profiling mode; other smaller ones are placed on moorings and mobile platforms (e.g., floats; see Sect. 18.3.2). This type of sensor package has been the major workhorse of the oceanographic community during the second half of the 20th century (reversing thermometers and water-sampling bottles were used before).

It is necessary to note that all three variables T , S , and P must be measured as near to simultaneously as possible, or with known time offsets, otherwise aphysical readings (density spiking) are obtained. In practice this means having the sensors as close together as possible and often pumping is used to create a predefined flowrate/time delay between sensors.

There is ongoing work to try to use optical methods to determine the index of refraction and thus the density directly. To date, though, the sensors either have excellent high-speed precision (but also respond to turbulent velocity signals, making it an optical *shear probe* as well) with little longer-term absolute accuracy, or are slow and have marginal absolute accuracy.

18.2.6 Velocity

There are three primary means of making point measurements of velocity: mechanical, acoustic, and electromagnetic. Mechanical current meters use rotors, vanes, and propellers, with compass cards to determine geomagnetic reference. They suffer from less than adequate response (e.g., stalling at low speed), low reliability, and high operating and maintenance costs. Because these are being phased out of use, the focus here is on the latter two methods.

The proceedings of the most recent quadrennial Institute of Electrical and Electronics Engineers (IEEE) Oceanic Engineering Society conference on current measurement technology [18.8] is a recommended source of the latest information on this and related topics. An earlier review of the subject is given by Collar [18.9].

Acoustic Current Meters

Acoustic current meters are of two basic types: time of flight and Doppler (Fig. 18.7). (There are many conceptual similarities between these instruments and their atmospheric equivalents, e.g., sonic anemometers; see Chap. 17.) Acoustic time-of-flight/travel-time (ATT) systems are based on the simple notion that sound travels faster with a flow than against; the differential travel time is a direct measurement of the flow velocity. At the

same time, the average of the two travel times in each direction gives the sound speed. The general expression for travel time is the integral along a ray path Γ with arc length s :

$$t = \int_{\Gamma} \left(\frac{ds}{C + u\tau} \right), \quad (18.5)$$

where C is the sound speed, and $u\tau$ is the velocity component projected onto the ray path.

Assuming that the current speed u is much less than a nominal background sound speed C_0 and a straight path of length R along the flow direction, one obtains for the differential and average travel times, respectively:

$$\delta t = -2u \left(\frac{R}{C_0^2} \right) \quad \text{and} \quad t = T_0 - \left(\frac{R}{C_0^2} \right) \delta C, \quad (18.6)$$

where T_0 is the nominal travel time along the path and δC is a sound speed (temperature) perturbation. For path lengths on the order 10 cm, a 1 cm/s resolution implies a 1 ns differential travel-time resolution. This can be achieved in three possible ways: direct measurement of broadband pulse travel time, phase difference, or frequency difference techniques. A representative ATT is shown in (Fig. 18.7). The supporting cage is meant for inline mounting in an oceanographic mooring. The four sensor heads are at the bottom. The specified accuracy is 2% of the reading or ± 1 cm/s up to 3 m/s, with a resolution of 0.1 mm/s. Absolute heading and tilt accuracy

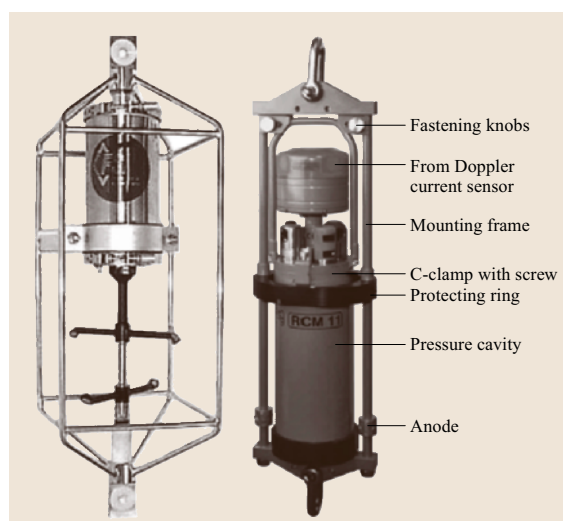


Fig. 18.7 Acoustic current meters: travel time (left, Fal-mouth Scientific 3-D ACM, Cataumet) and Doppler (right, Aanderaa RCM-11, Bergen)

are 2° , measured with a three-axis flux gate system and two accelerometers. The maximum sample rate is 2 Hz. A thermistor measures water temperature to obtain the sound speed.

The need for a mechanical supporting structure presents two problems. To prevent vibration from contaminating the velocity measurement, the structure must be rigid. To prevent structure-generated flow perturbations from contaminating the result, the redundant paths can be selectively sampled to include only those on the *upstream* side.

In custom applications these techniques have been extended to 3 m path length, operating for five years under a surface buoy without a problem. The latter highlights an advantage of acoustic techniques in ocean observations – the robust nature of the hardware and insensitivity to calibration problems.

The acoustic Doppler current meter transmits an acoustic pulse and measures the frequency shift of energy reflected or scattered off particles in the water. It does not matter if the particle impedance is higher (as for sediment particles) or lower (as for air or gases); both will result in a reflection.

The water velocity is determined from the measured Doppler shift f_D , the frequency difference between the transmitted and received signals using the equation

$$u = \frac{1}{2} C \frac{f_D}{f}. \quad (18.7)$$

To obtain a velocity vector, data from several beams are combined. The beam geometry varies, some diverge and assume locally homogeneous flow while others cross to measure in a small volume, much like a laser Doppler velocimeter.

Because the frequencies used are typically quite high in these short-range applications (e.g., 2 MHz) and the Doppler shifts are small (30 Hz for 1 cm/s) there is no problem with resolving low velocities as they are small perturbations about the carrier. When particle scattering strength is low, the signal-to-noise ratio will be low, but it will be unbiased. Ambient acoustic noise at these frequencies is due to thermal fluctuations only and is white. The conversion of the measured Doppler shift to velocity depends only on the speed of sound, which is adequately known with an independent measurement sensor (transmit and receive circuits share a common oscillator, so errors in drift cancel). Again, because there are no moving parts, the instrument is inherently reliable. If in a moored configuration, the motion of the mooring could influence the interpretation of the measurements.

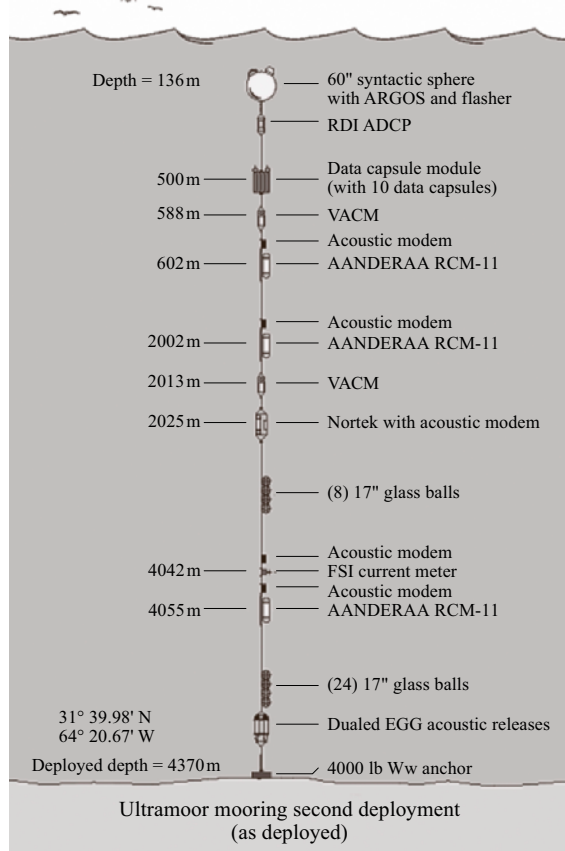


Fig. 18.8 The Ultramoor with various current meters, acoustic modems, and data capsules for data return. RDI (RD Instruments, Inc.), VACM (vector averaging current meter)

In an example of an oceanographic mooring with many current meters (Fig. 18.8), the mooring reaches from the seafloor 4370 m deep to close to the surface (a subsurface mooring avoids wave stresses and associated motion). This particular mooring is part of the Ultramoor program at the Woods Hole Oceanographic Institution, specifically meant to test data capsules and acoustic modems [18.10].

Electromagnetic Current Meters

A conducting fluid moving through a magnetic field generates an electric field that is dependent on the fluid velocity – a statement of Faraday's law of magnetic induction. In current meters, the magnetic field is generated by an alternating-current (AC) excitation in the instrumentation. In larger-scale applications, ocean flow

Fig. 18.9 An electromagnetic current meter in a frame for bottom use (InterOcean S-4, San Diego)



through the Earth's magnetic field generates a voltage often measured using submarine cables (see below). For the ocean case, the voltage E in the water is the product of the water flow velocity u , the magnitude of the magnetic field B , and the length of the conducting path L :

$$E = uBL . \quad (18.8)$$

In a common electromagnetic current meter (Fig. 18.9) the magnetic field intensity is generated by a circular coil, internal to the instrument, driven by a precisely regulated alternating current. Two orthogonal pairs of titanium electrodes located symmetrically on the equatorial ring of the instrument sense the respective voltages and the separation defines the path; data from a flux gate compass is used to calculate the current vector with respect to north.

The flow field around the sensor heads is of critical importance. The grooved surface of the housing produces stable hydrodynamic characteristics by inducing a fully turbulent boundary layer with uniform and stable vortex shedding through the range of use. This ensures a stable and linear calibration. (Recall the sensitivity of electric field lines to geometry as discussed in Sect. 18.2.3). The specifications are: range 0–350 cm/s, accuracy 2% of reading or ± 1 cm/s, sampling rate 5 Hz, resolution 0.04 cm/s, noise 0.05 cm/s root-mean-square (rms) for 10 s averages, and direction $\pm 2^\circ$. Because of the AC excitation there is no zero-velocity threshold. Biofouling can affect the calibration, though. Such sensors do not lend themselves to turbulence measurements because of the weighted volumetric averaging.

18.3 Lagrangian Techniques

The most basic Lagrangian data is position as a function of time, from which velocity can be calculated. This is true whether a parcel of dye is being followed or a float is following a flow. In the latter case, the sensors the float platform carries (typically) contribute moving point measurements. The interpretation of the data can be complicated by this space–time mix of information.

18.3.1 Surface Drifters

The design of surface drifters is driven by the need to faithfully follow the flow in a known and repeatable way, and at the same time is influenced by considerations of cost, ease of storage and deployment (around the world in large numbers, from ships and planes), robustness, and longevity. Systematic evaluations of the different surface drifter designs of the 1980s concluded that the key to accurate water following was to increase the ratio of drogue to float size. Much iterative work was done to determine optimal designs, and there is some convergence.

For the open ocean the surface velocity programme (SVP) drifter has a spherical plastic float, a wire tether, a holey sock drogue (a 4 m-long canvas cylinder centered at 15 m depth), and battery power sufficient for two years of operation (Fig. 18.10). SVP drifters can carry sensors that measure temperature and salinity, wind direction, ambient sound (to calculate wind speed and rain rate), upwelling light, and atmospheric pressure; most though only carry sea surface temperature and atmospheric pressure sensors. Advanced research and global observation satellite (ARGOS) receptions (for data transfer and positioning) vary from 6 to 14 per day, depending on latitude and storm conditions. About 7500 SVP drifters have been deployed since 1988.

A drifter originally developed for the coastal ocean dynamics experiment in the 1980s has had greatest use in coastal and marginal sea deployments. It can be deployed from a small plane, helicopter, or boat. Location is by GPS or ARGOS. Data transmission is to ARGOS or a local paging system on land. Two types are manufactured, one with a spherical float and a radar corner reflector-style drogue, the other with a cruciform drogue

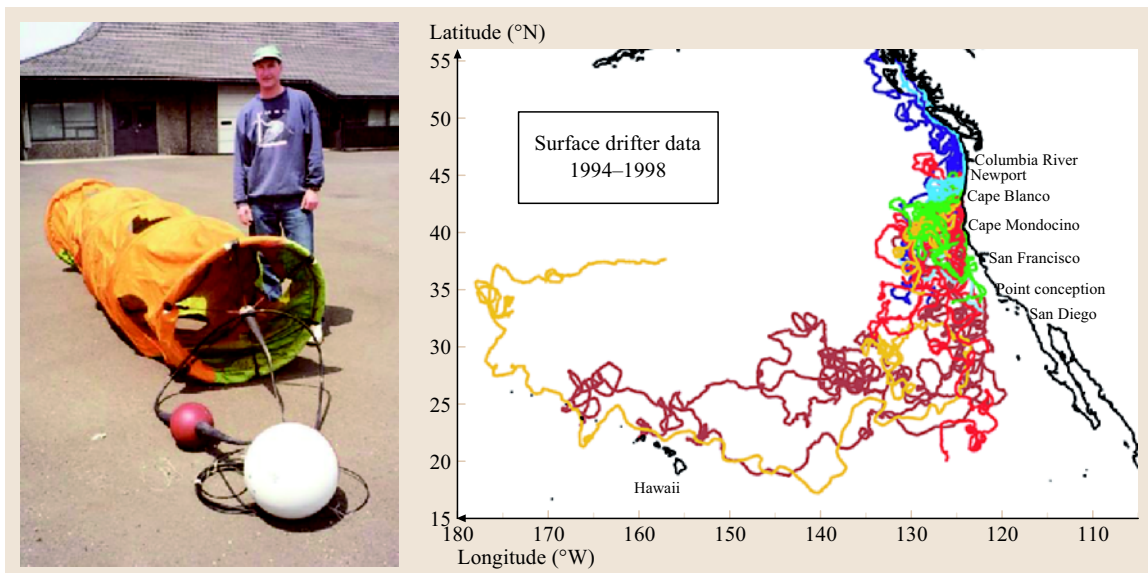


Fig. 18.10 (left) An SVP drifter. (right) Paths of surface drifters released off the Oregon coast in spring and early summer (red, yellow, and brown), late summer and fall (green and light blue), and winter (dark blue). (courtesy of J. Barth)

with four small floats. Temperature and salinity sensors have been placed on these drifters. A power recharging option is available, making them redeployable after recovery. About 2500 drifters of this type have been deployed in the past 10 years.

18.3.2 Deep Ocean Floats

The use of neutrally buoyant and profiling floats has been a cornerstone of oceanography for the last half century, and this will continue. In the late 1950s swallow

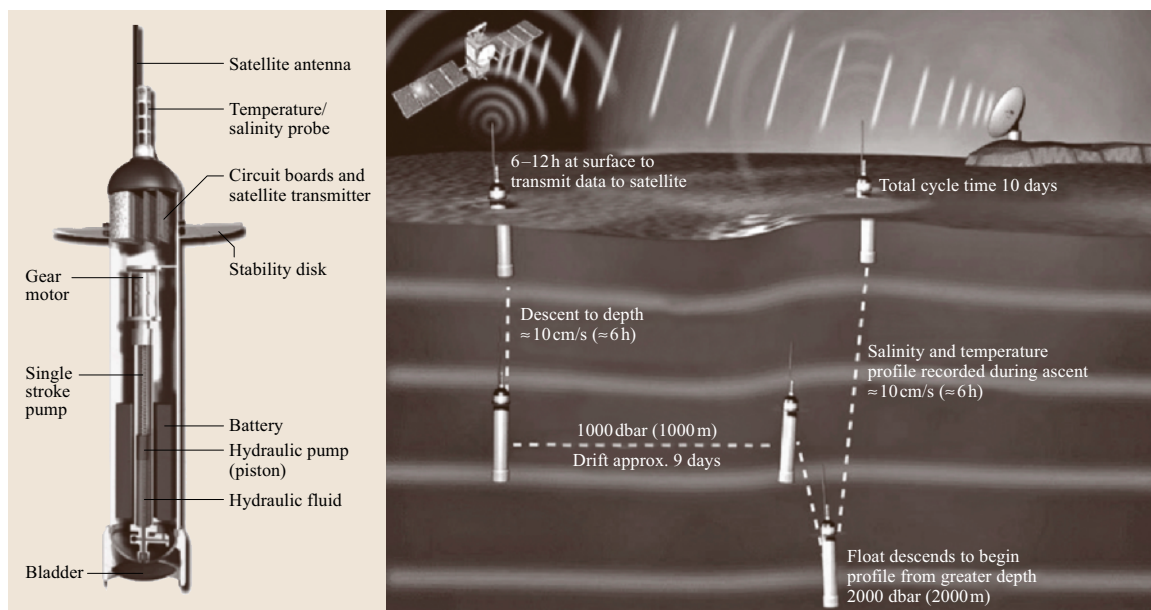


Fig. 18.11 Argo float (16 cm diameter, 130 cm long, 26 kg)

floats misbehaved by moving at *high* speed (10 cm/s) in seemingly random directions rather than slowly in a straight line (baffling the crew on the sailboat trying to track them acoustically), thus awakening oceanography to the presence of mesoscale ocean *weather*.

The key to constructing such floats is to ensure that the float's density, and especially the floats compressibility, accurately matches that of the seawater in which they float. Doing this not only lets them float at the desired depths and faithfully follow fluid accelerations, but also minimizes power needed to profile. Early floats were aluminum scaffolding tubing; in some cases, special hulls of glass (a large *test tube*) or numerically machined, ribbed cylinders were used. In any case, careful ballasting of each individual float (grams out of many kilograms) is required.

There are two basic modes of operation for freely drifting autonomous floats: acoustically tracked and profiling (and combinations). Profiling floats such as Argo (Fig. 18.11) typically come to the surface once every 10 days to telemeter temperature and salinity data and to obtain a satellite navigation fix. During the time submerged the float is typically untracked. These floats change and adjust their buoyancy using a piston to move oil in and out of a bladder exposed to the seawater. Their lifetime is about four years or 150 profiles. The goal of the international Argo program is to seed the ocean with 3000 floats to obtain on average one float every 300 km (750 floats/y); at the end of 2004 there were 1500 floats in operation around the world. This is a major effort being undertaken by the international community. While the initial emphasis was on temperature and salinity, additional sensors are being added for dissolved oxygen, horizontal electric field for velocity, and hydrophones for wind and rain (and seismic and marine mammal sound), to name a few.

A widely used and accurate method to study the ocean in motion employs the deep sound, or sound fixing and ranging (**SOFAR**), channel to track neutrally buoyant drifters over large horizontal distances, on the order of 10×10^3 km. Three or more anchored sound sources provide an acoustic navigation system whereby precisely timed acoustic signals [in this case, an 80 s-long 1.5 Hz-wide frequency-modulated (FM) sweep at 260 Hz] spread out radially from each of the sources. Given the arrival times at a drifting receiver equipped with a synchronous clock, the receiver's position can be determined to an accuracy of a few kilometers or better. Since the mid 1980s floats have been deployed in many different projects worldwide to study ocean currents.

These floats, also known as RAFOS floats (**SOFAR** spelled backwards), can be deployed to drift at any depth, although greater acoustic ranges are possible if both the sound sources and the floats are not too far from the sound channel axis. The floats record the arrival times in their microprocessor memory. At the end of each float's mission underwater, it surfaces and telemeters all its data back to shore. Typical missions last from months to several years. Special float designs have been developed whereby a float surfaces briefly to telemeter its data before returning to depth to continue its underwater mission. To make the floats mimic fluid motion accurately, they can be configured to drift with the water both horizontally and vertically; these are known as isopycnal floats. In regions of high shear, profiling floats can give erroneous estimates of velocity if they are based solely on surface fixes. Similarly, when trying to measure abyssal currents, estimates can be severely compromised if the float comes to the surface. In these cases it is advantageous to remain submerged. Some systems are *turned around* using fixed receivers and drifting sources (**SOFAR** floats).

One illustrative application of navigated floats was in the Atlantic climate change experiment (ACCE, Fig. 18.12) where the float provided *in situ* observations of dissolved oxygen. Here the sensors were only briefly activated, once daily, and thus operated over the entire lifetime of the floats. From a Lagrangian viewpoint, interpreting the variability of dissolved oxygen presents the difficulty of separating the biological from the physical processes. However, there are times when the nature of the variability clearly indicates that one process dominates the other.

18.3.3 Dispersion

Tracer release experiments use methods to estimate directly the dispersion and mixing across density interfaces (diapycnal diffusivity) in the ocean. Although logistically challenging, the method is straightforward: a passive tracer or dye is injected at depth (on a density surface), typically from a vessel, and an initial survey is done to map the tracer distribution. The region is resampled at discrete time intervals, and the goal for each survey is to map a large enough region to account for all of the tracer. The measurements are used to estimate the time- and space-averaged diapycnal diffusivity for the region. (Dispersion in the atmosphere is discussed in Sect. 17.2.)

For deep-ocean tracer release experiments lasting several years, sulfur hexafluoride (SF_6) has been

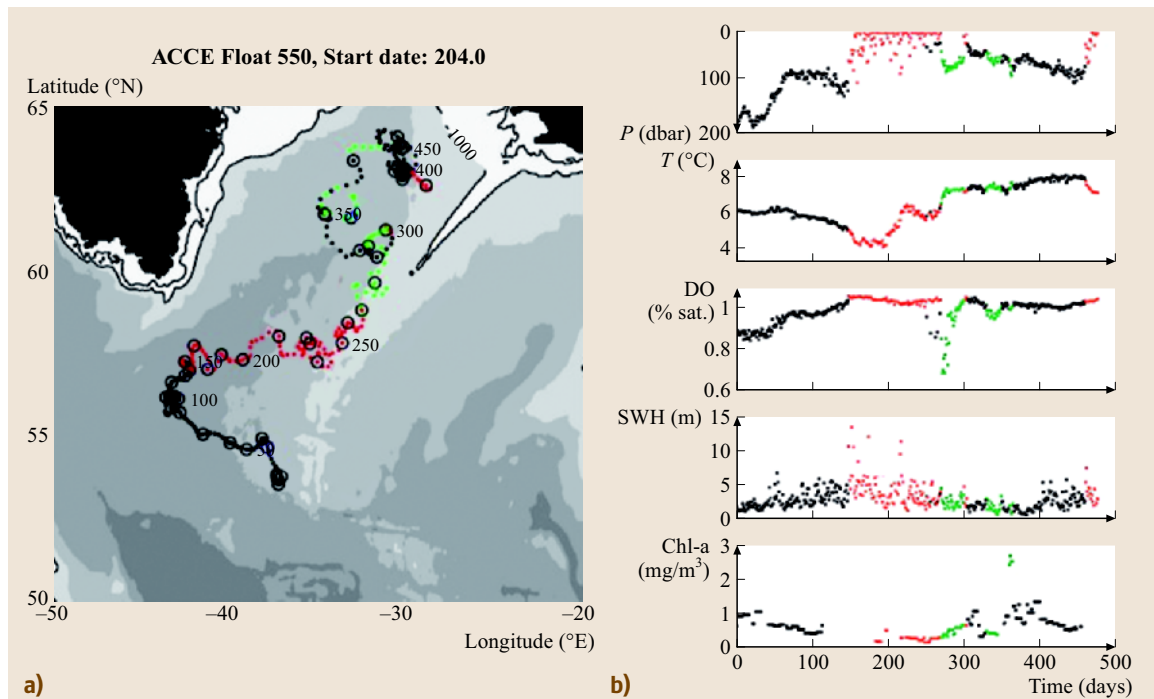


Fig. 18.12 The track (left) of an isopycnal float that outcrops in the Irminger Sea with the corresponding measurements of pressure, temperature, and dissolved oxygen (right) (courtesy of T. Rossby)

the tracer of choice [18.11–13]. Its background concentration in the marine environment is low, it is chemically conserved, and it is harmless to marine organisms [18.14]. However, SF₆ is becoming a useful anthropogenic tracer in studies of the pathways from the atmosphere into the ocean interior, and therefore replacement tracers are being sought. Trifluoromethyl sulfur pentafluoride (CF₃SF₅) has similar properties to SF₆ [18.15], but its background in the atmosphere is too low for it to be useful as a transient tracer; it may be a viable alternative to SF₆. The method of injection is the same for both gases; the gas is forced through atomizing orifices so that droplets dissolve before sinking about one meter below the release density surface. The gas is pumped continuously to an injector sled towed behind a slowly moving ship. The sled tracks a density surface using automatic feedback control from a CTD sensor mounted on the sled. Subsequent sampling uses a towed vertical array of water samplers and temperature-pressure sensors; samples are analyzed using a gas chromatograph equipped with an electron capture detector. The minimum detectable amount for both gases is about 0.01 femtmoles. The achievable sampling

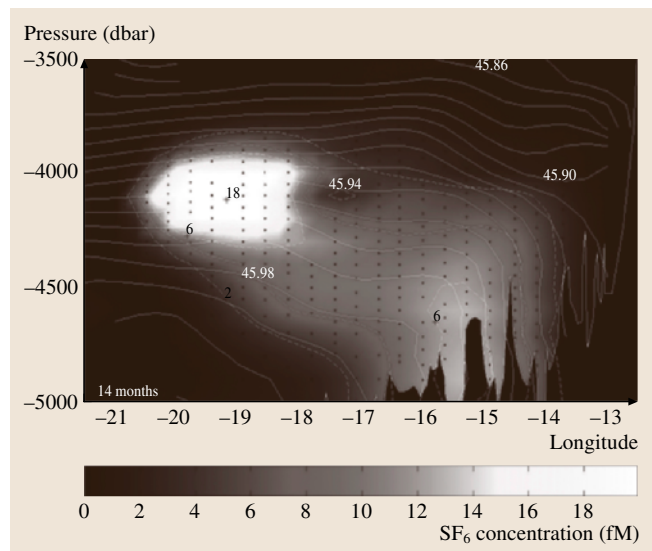


Fig. 18.13 SF₆ concentration 14 months after release in the Brazil Basin [18.16]

rate using shipboard gas chromatograph is of order 200 samples/d.

The Brazil basin tracer release experiment provides an example of the method [18.16]. (Fig. 18.13) shows the concentration of SF₆ 14 months after release in early 1996. This data, when coupled with independent measurements of the dissipation rate of turbulent kinetic energy, support the hypothesis that the tides running over the rough bathymetry generate internal waves that propagate upwards into the water column where the associated shear intensifies, inducing turbulent mixing events.

Fluorescent dyes are used for experiments where higher sampling rates, on the order of 5 Hz, are required

to resolve processes that have time scales of hours to days [18.17]. Although the minimum detectable level in this mode is about a million times higher than for SF₆, these dyes are superior for small volumes (about one cubic kilometer) and short durations (five days). Fluorescein, Rhodamine-WT, and Rhodamine-B are examples of commonly used dyes. Rhodamine-B is a suspected carcinogen; the other two are both nontoxic. Fluorescein is preferable to Rhodamine-WT in that it is less expensive and the background levels are much lower, but it decays rapidly in sunlight whereas WT is stable.

18.4 Remote Sensing

Remote sensors measure wave signals that are generated or modified by ocean processes at some distance. For the ocean case there are two classes: in situ and external. In the first, acoustics and electromagnetics are usually implied, often simply extending the range of what were called point measurements. The latter usually refers to the electromagnetic sensing of the sea surface, whether using radars from land or other sensors probing the ocean surface from space satellites. In atmospheric measurements, sonic detection and ranging (SODAR), light distance and ranging (LIDAR), and atmospheric GPS tomography are conceptually similar remote sensing methods (Sect. 17.3).

18.4.1 Acoustic Doppler Current Profilers (ADCP)

Acoustic Doppler current profilers (ADCPs) are multi-beam Doppler SONARs used to measure ocean currents. They have several advantages over point current meters: they measure a profile of currents, have no moving parts (and so are not susceptible to stalling or mechanical fouling), and are nonintrusive.

ADCPs have come into widespread use since the technology was first introduced [18.18, 19] and different types of profilers have evolved for different applications. The range, resolution, and accuracy of the measurements depend upon the frequency of the ADCP and on sampling and environmental factors; some of the main considerations are discussed below, although it is impossible to be comprehensive here. ADCPs are used from a variety of platforms: current meter moorings, ships (through the hull, over the side, or towed), autonomous undersea vehicles (AUVs), in bottom-mounted configurations, or lowered through the water on a wire, to

name a few. Because the ADCP measures only the velocity of the water relative to the instrument, the velocity of the instrument relative to the Earth must also be measured accurately. Hence it is important to include the measurement platform as part of the overall ADCP system.

An ADCP transmits a pulse of high-frequency sound (a ping) along multiple acoustic beams and estimates the Doppler shift in frequency of the sound reflected from scatterers in the water over successive time intervals (range gates) corresponding to the distance (range) from

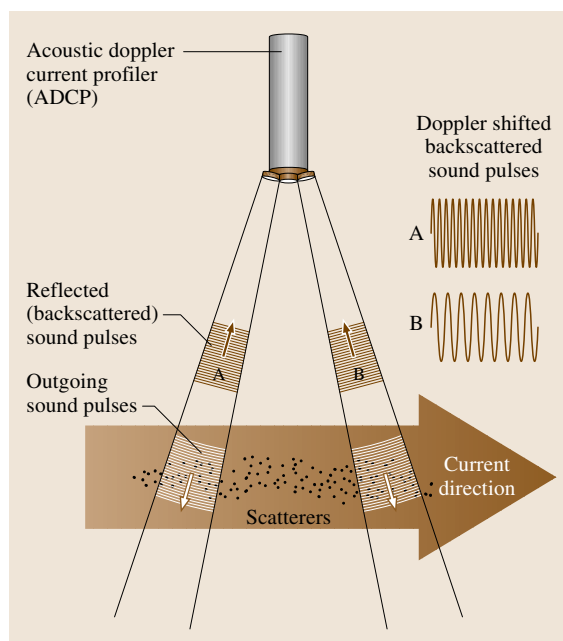


Fig. 18.14 The ADCP principle of operation

the transducer to the scatterers (Fig. 18.14). At the frequencies commonly used (from ≈ 10 kHz to ≈ 10 MHz), the scatterers are primarily plankton and small particles that are assumed to be passively advected by the currents. The Doppler shift in frequency is proportional to the along-beam velocity of the scatterers relative to the transducer (18.7),

$$f_D = \frac{2f_t u_b}{C}, \quad (18.9)$$

where f_D is the Doppler shift, f_t is the transmit frequency, u_b is the velocity component along the beam, and C is the speed of sound in seawater. The beam geometry and the transducer orientation are used to convert beam velocities into Earth components: east, north, and vertical. A minimum of three beams is required to determine a three-dimensional velocity vector. In practice, a four-beam configuration is common, spaced at 90° in azimuth and at a fixed angle with respect to vertical. Figure 18.14 illustrates the principle for one beam pair. A current flowing from left to right will have a component towards the transducer along beam A and away from the transducer along beam B. If the current is uniform over the distance spanned by the beams, the Doppler shifts of the transmit frequency will be of equal size but opposite sign. Two beams determine the horizontal and vertical velocity in the plane defined by the beams. A second pair is used to determine the orthogonal component of horizontal velocity and a redundant estimate of vertical velocity.

A basic assumption of the technique is that the scatterers are present and that they are passively advected by the currents. In the ocean the distribution of scatterers varies both geographically and with depth. Scatterers are often not uniformly distributed with depth; they are layered, alternating from high concentrations to low, and there is typically a dramatic decrease at depths exceeding about 1000 m. Scattering layers can introduce bias in **ADCP** current measurements in a number of ways. First, they may swim, and a prime example is diel vertical migration at sunrise and sunset [18.20]. Second, very strong scattering layers serve as a hard reflector, like the bottom, and can bias the current measurement. Detecting bias and editing it out is one of the primary data quality screenings that is applied in post processing.

ADCPs can be categorized by type of acoustic pulse. Pulses can be coded (broadband) or uncoded (narrow band). A narrow-band **ADCP** transmits pulses that are gated sinusoids and measures the Doppler frequency shift of the echoes. Narrow-band **ADCP** bandwidth and accuracy are inversely proportional to the pulse dura-

tion. A broadband **ADCP** transmits pulses modulated with pseudorandom codes and estimates the Doppler phase shift of the echoes in the range $\pm 180^\circ$ [18.21]. Broadband bandwidth and accuracy are directly proportional to code length. The ambiguity velocity is the largest velocity that can be measured by a broadband **ADCP**, as phase wraps of 360° cannot be distinguished. Ambiguity velocity is an important issue for systems mounted on platforms that move at great speeds relative to ocean currents, e.g., vessel mounted, as the **ADCP** needs to resolve the velocity of the water relative to the ship (5–6 m/s) even though the ocean currents of interest rarely exceed 1 m/s. Increasing the maximum ambiguity velocity requires decreasing the code length and therefore bandwidth and accuracy. Broader bandwidth also reduces the maximum range and increases the chance of acoustic interference from other devices. Hence, although a broadband **ADCP** has the potential for better short-term accuracy than a narrowband **ADCP**, there are other tradeoffs that need to be considered for any particular application.

The basic transducer styles are monolithic and phased array, and either type can be driven with broadband or narrow-band pulses. A monolithic piston transducer consists of a single piezoelectric ceramic disk that generates one beam. A phased-array transducer consists of an array of small ceramics wired such that alternate columns or rows can be driven with different time delays, generating two or four beams simultaneously. Transducer style is often an issue when seeking to maximize the velocity profiling range. Lower-frequency SONARs get better range because the attenuation and absorption of sound in seawater is lower at lower frequency. Because the angular beam width varies inversely with the product of the frequency and the transducer width, a lower frequency corresponds to a larger transducer size for a fixed beam width. Large transducers are more expensive to manufacture and more cumbersome to deploy. At low frequency, a phased-array transducer can be more practical than a multibeam monolithic style transducer because it is smaller, generating multiple beams from a single transducer. It is more complicated and expensive to manufacture, however, and variations among the ceramic elements will degrade the beam pattern.

The limiting factor affecting the short-term accuracy of **ADCPs** is the theoretical bound on the random error [18.22], but the overall accuracy of the current measurement is determined by the sum of all random and bias errors of the **ADCP** system, i.e., **ADCP** plus platform motion. To use a specific example, a commonly

used commercial **ADCP** is a 150 kHz narrow-band **ADCP** manufactured by RD Instruments. At 8 m vertical resolution, the single-ping standard deviation of horizontal current from this instrument is approximately 11 cm/s. Vector-averaging over 600 s intervals reduces the standard deviation to less than 1 cm/s [18.23]. Hence, in the absence of any system biases, the predicted error for averaged currents using this instrument mounted on a rigid platform is quite small compared to the variance of the currents being observed. When used to profile currents from a ship underway, however, the errors are dominated by the accuracy of determining the ship's motion. The ship-relative currents measured by the **ADCP** must be rotated into Earth coordinates using a measurement of ship's heading, and the ship's velocity over the Earth must be subtracted. Because the ocean current is a small residual between the rotated **ADCP** measurement and the ship speed, the calculation is particularly sensitive to errors in heading and/or transducer alignment. A heading bias of one degree for a ship steaming at 5 m/s can introduce an error of 9 cm/s in the cross-track component of horizontal velocity. Heading

bias errors, formerly the most limiting error in shipboard profiling, have been largely eliminated by the use of **GPS** attitude measurements [18.24, 25]. With excellent **GPS** position and heading measurements, the accuracy of ocean currents from shipboard **ADCP** measurements can achieve an accuracy of 2 cm/s for 600 s averages [18.26].

The **ADCP** has numerous advantages over point current meters, and it is used routinely on moorings and in bottom-mounted configurations. Direction and orientation are determined from an internal magnetic compass and pendulum tilt sensors. In addition to profiling currents, the **ADCP** provides a remote sensing measure of the scattering layer, useful in estimating biomass [18.28]. High-frequency **ADCPs** can be used to estimate turbulence [18.29, 30].

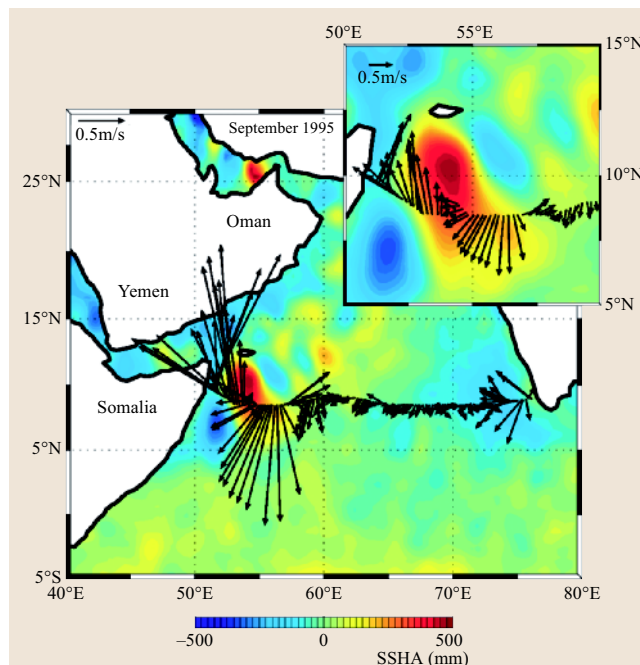


Fig. 18.15 Currents at 22 m depth measured from the R/V *Knorr* during the 1995 Arabian Sea southwest monsoon, overlaid on sea surface height anomalies from altimetry [18.27]. The Great Whirl is the large anticyclonic eddy centered at 55°E (positive sea surface height anomaly)

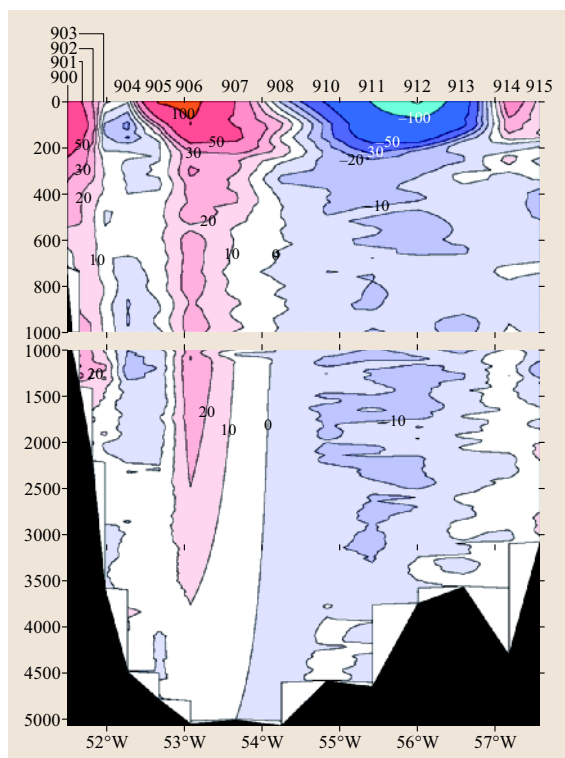


Fig. 18.16 Cross track component of current measured from the R/V *Knorr* during the 1995 Arabian Sea southwest monsoon. The section merges current observations in the upper 400 m made from continuous underway shipboard **ADCP** and lowered **ADCP** observations made at stations located at positions indicated by numbers along top axis. The Great Whirl is seen to have significant current strength to about 2000 m depth

Shipboard profiling was one of the earliest uses of the **ADCP** [18.31, 32]. The advent of **GPS** with its greatly improved accuracy of position and heading measurements helped to establish the shipboard **ADCP** as a standard survey tool. Horizontal resolution is 3 km (for typical ship speeds); range is limited by the frequency. A 150 kHz **ADCP** (e.g., (Fig. 18.15)) profiles to 400 m depth in good scattering conditions.

The lowered **ADCP** is an adaptation to extend the profiling range to full ocean depth [18.33, 34]. A self-contained **ADCP** such as used on a mooring is mounted on a package usually containing a **CTD** and lowered from the surface to the ocean floor. A set of overlapping profiles of horizontal currents are obtained, each with a range of about 100–200 m that are first differenced, averaged, and gridded to form a full depth profile of horizontal velocity shear. The shear or relative velocity profile is referenced in a similar manner to the shipboard **ADCP**, using accurate **GPS**. Figure 18.16 shows a vertical section of cross-track currents measured from R/V *Knorr* along the track shown in (Fig. 18.15). The upper 400 m was measured by shipboard **ADCP**; at greater depths the currents were measured by lowered **ADCP** observations made at the fixed station locations indicated along the top.

18.4.2 Acoustic Tomography

Sound travels faster in warm than in cold water. By measuring the travel time of sound over a known path, the sound speed and thus the temperature can be determined. Sound also travels faster with a current than against. By measuring the reciprocal travel times in each direction along a path, the absolute water velocity can

be determined. Each acoustic travel time represents the path integral of the sound speed (temperature) and water velocity (18.5). As the sound travels along a particular ray path, it inherently averages these properties of the ocean, heavily filtering along-path horizontal scales shorter than the path length. Over a 1000 km range, a depth-averaged temperature change of 10 m°C is easily measured as a 20 ms travel-time change [18.35].

In ocean acoustic tomography travel time data from a multitude of paths crossing at many different angles are used to reconstruct the sound speed (temperature) and velocity fields (Fig. 18.17). The projection slice theorem requires views from many angles to fill in Fourier wavenumber space, and thus be able to map physical space via an *inverse*. The many crossing paths determine the spatial resolution, and differences in travel times give the strength of the perturbations.

Figure 18.17 illustrates an important characteristic of tomographic systems. For N instruments the number of paths and corresponding data is $N_{\text{paths}} = 1/2N(N - 1)$. For example, there are eight instruments in the figure, resulting in 28 paths (not all shown); if one more instrument is added 36 paths results with an increase of eight data for only one additional instrument. This quadratic growth of data with the number of instruments is one reason why instruments only on the periphery can obtain high resolution in the interior.

An oceanic vertical sound speed profile and a set of acoustic rays for 620 km range are shown in (Fig. 18.18). Because of the competing effects of decreasing temperature and increasing pressure with depth, a sound speed minimum occurs at about 1 km depth. This deep-ocean sound channel (mentioned above in the navigation context), or waveguide [with an index of refraction of C/C_0 ,

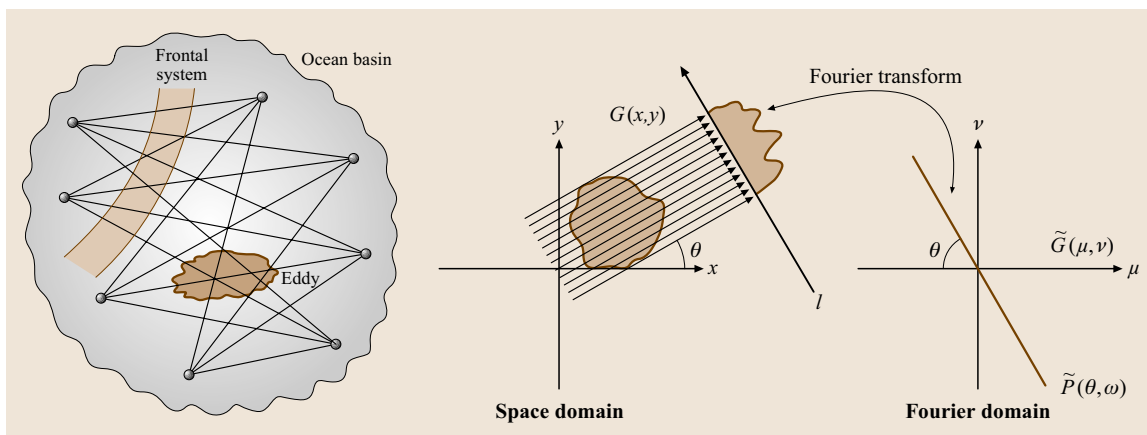


Fig. 18.17 (left) Acoustic paths going through eddies and fronts, and (right) the projection slice theorem

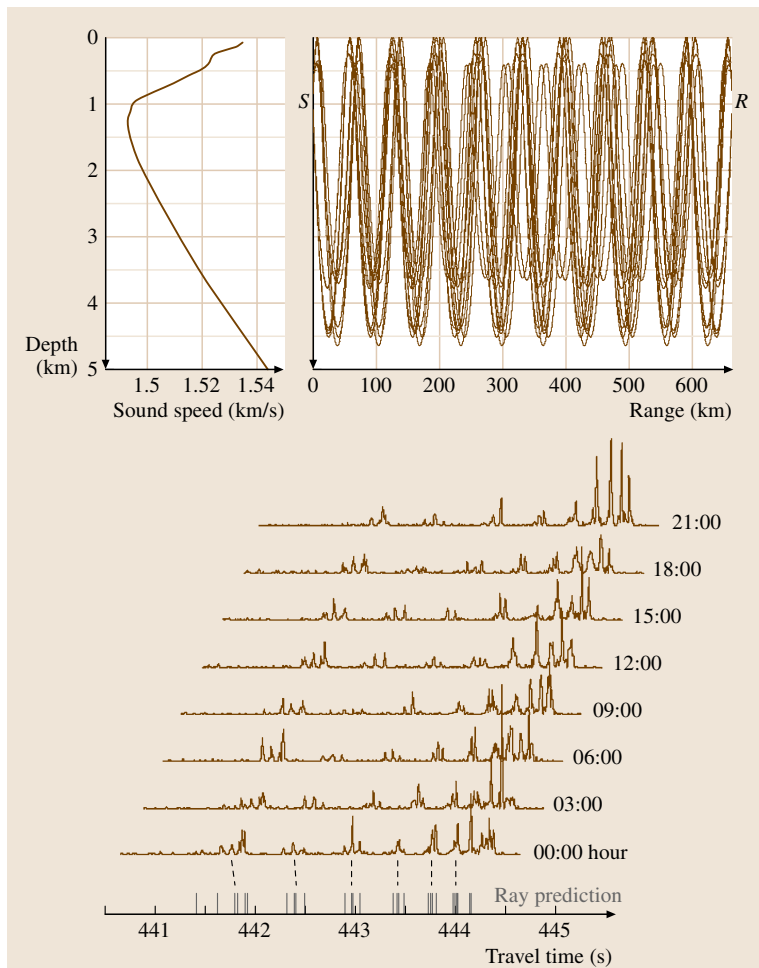


Fig. 18.18 Sound speed profile, acoustic eigenrays, and predicted and measured travel times for a range of 620 km

where C_0 is the minimum sound speed $\approx 1490 \text{ m/s}$ at a depth of 1000 m in (Fig. 18.18)], causes acoustic energy to be trapped in the water column so that it can propagate great distances without interacting with the ocean bottom. The sound channel also results in multiple acoustic paths, called *eigenrays*, between an acoustic source and a receiver. The eigenrays have different travel times because they traverse water with different sound speeds and the path lengths are different. The acoustic receiver detects the arrival of multiple pulses, and each pulse can be identified with a predicted eigenray. The figure shows the measured predicted arrival patterns for a 620 km path south of Bermuda. The World Ocean Atlas [18.36] was used to make the predictions. Recorded arrivals are slightly earlier than predicted, suggesting that temperatures were above their climatological mean.

Recasting (18.5) and (18.6) results in the perturbation expression:

$$\delta t = \frac{-R}{C} \left(\frac{\delta C}{C} - \frac{u}{C} - \frac{\delta R}{R} \right), \quad (18.10)$$

where δt is the travel-time perturbation due to small perturbations in sound speed δC , range δR , and water velocity u along the path. As mentioned above, for a $10 \text{ m}^\circ\text{C}$ temperature perturbation $\approx 0.04 \text{ m/s}$ sound speed perturbation over a 1000 km path, with $C = 1500 \text{ m/s}$, the perturbation travel time is $\approx 20 \text{ ms}$, which is measured easily when averaged over several transmissions in one day.

Clearly precise timekeeping and instrument positioning are required, on the order of a millisecond and one meter for experiments with ranges $> 100 \text{ km}$. The former is accomplished using either a GPS timing sig-

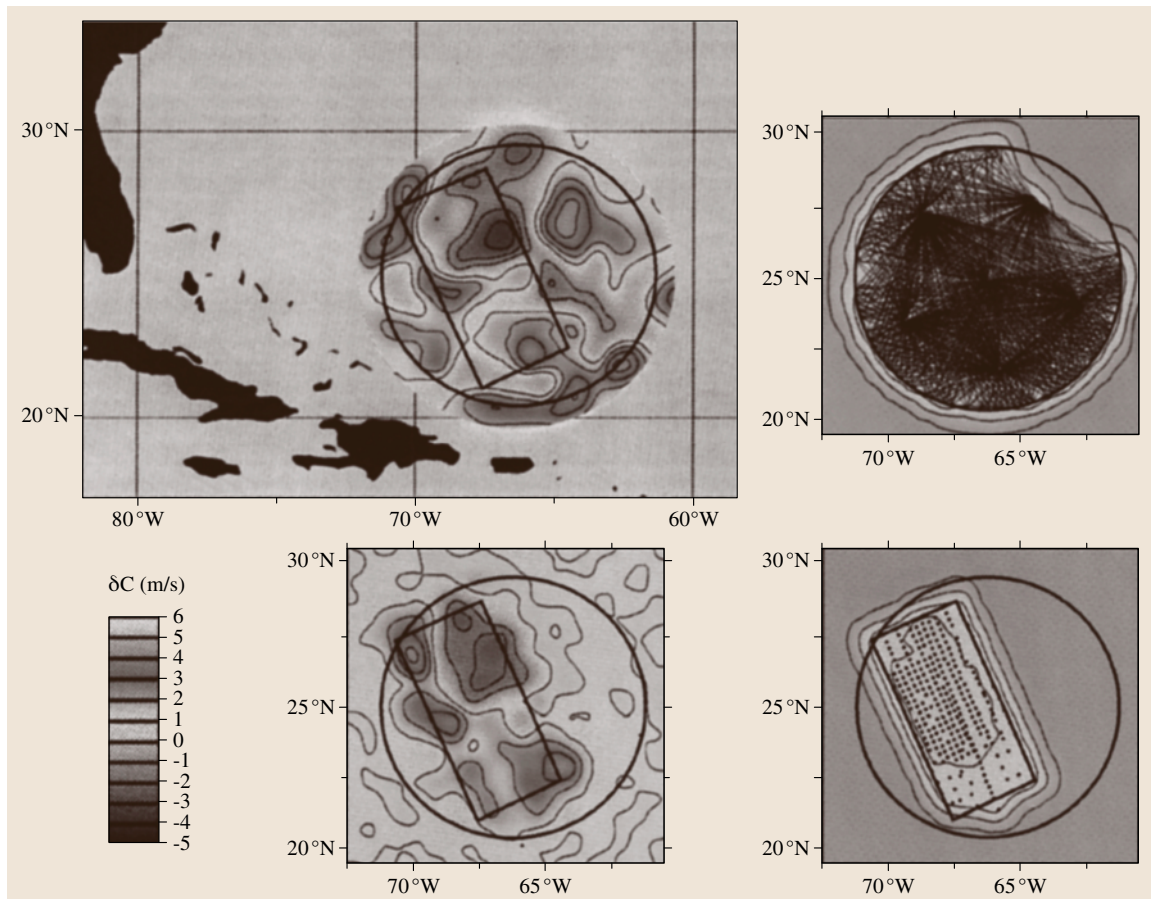


Fig. 18.19 Acoustic tomographic mapping of the ocean

nal if available, or a low-power crystal clock combined with a low-duty-cycle high-power rubidium frequency standard. If the source is moored on the bottom, possibly swaying in the *ocean breeze* 4 km above the bottom, precise navigation is usually accomplished with a local long-baseline high-frequency (10 kHz) acoustic navigation system (a pinger on the mooring ranging off transponders on the seafloor).

Most acoustic sources used for oceanography are limited by transducers and power considerations to source levels $< 195 \text{ dB re } 1 \mu\text{Pa}$ (260 W). To obtain a high enough signal-to-noise ratio, pseudorandom codes are transmitted over long duration at relatively low power; the received signals are replica-correlated with a version of the transmitted signal with the result a single peak. Code processing gains are usually on the order of 30–40 dB, with the limit determined by ocean fluctuations that limit the coherent averaging times. Var-

ious frequencies are used depending on range: 20 Hz and 75 Hz for a multi-megameter, 250 Hz for $< 1 \text{ Mm}$, 400 Hz for $\approx 300 \text{ km}$, and 5 kHz for 20 km.

Since it was first proposed in the late 1970s [18.37, 38], ocean acoustic tomography has evolved into a remote sensing technique employed in a wide variety of physical settings [18.39]. In the context of long-term oceanic climate change, acoustic tomography provides integrals through the mesoscale and other high-wavenumber noise over long distances. In addition, tomographic measurements can be made without risk of calibration drift; these measurements have the accuracy and precision required for large-scale ocean climate observation. Trans-basin acoustic measurements offer a signal-to-noise capability for observing ocean climate variability that is not readily attainable by an ensemble of point measurements. On a regional scale, tomography has been employed to observe active convection,

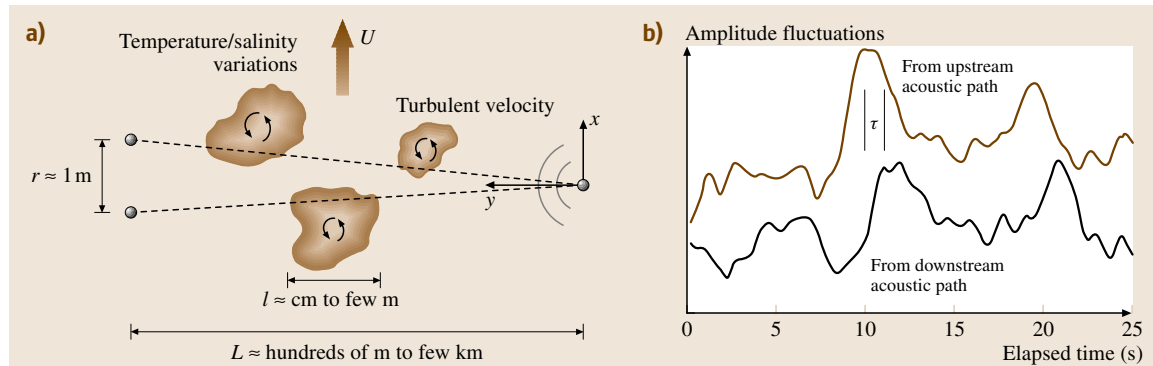


Fig. 18.20 (a) Acoustic propagation from a single source to two receivers. (b) Amplitude fluctuations at the two receivers show a time lag τ that corresponds to the time it takes for turbulence structures to cross the acoustic paths (courtesy of D. Di Iorio)

to measure changes in integrated heat content, to observe the mesoscale with high resolution, to measure depth-independent barotropic currents in a unique way, and to observe directly oceanic relative vorticity. The remote sensing capability has proven effective for measurements under ice in the Arctic and in regions such as the Strait of Gibraltar, where conventional in situ methods may fail. Coastal, shallow-water tomography is possible, though acoustic bottom interaction poses challenges. The acoustic paths are sensitive antennae for specific wavenumbers of the ocean wave field; the measurement technique is the only accurate in situ method to measure open-ocean barotropic and baroclinic (depth-dependent) tides [18.40]. This work led to a renaissance in the study of tides and ocean mixing (Sect. 18.6.1).

One of the original goals of tomography was to observe synoptically the mesoscale variability of the ocean. The acoustic mid-ocean dynamics experiment: moving ship tomography (**AMODE-MST**) obtained high-resolution, nearly synoptic three-dimensional maps of the ocean over a large area [18.41]. During 50 days in June and July 1991, a ship circumnavigated a 1000 km-diameter array of six moored acoustic sources, deploying a vertical receiving array every 3 h every 25 km to receive the signals from the sources (Fig. 18.19). The travel-time data along the many acoustic paths crossing at many different angles were then used to reconstruct the ocean sound speed (temperature) field in a way very analogous to a medical computed tomography (**CT**) scan. Sound speed perturbations at 700 m depth on the order of $1 \text{ m/s} \approx 0.25^\circ\text{C}$ were mapped [(Fig. 18.19), top left]. The acoustic travel time data were inverted to produce this field. For independent verification and comparison purposes, air-expendable

bathythermograph (**AXBT**) data (July 18–22) were collected and mapped [(Fig. 18.19), lower left]. The panels on the right show the line-integral or point sampling that was used to obtain the maps on the left, with estimated errors. The two estimates of the sound speed are within the uncertainties of each method. This experiment demonstrated that high-resolution maps could be obtained with this technique in the ocean, and that the navigation challenges could be overcome.

A limiting case of tomography is an inverted echosounder (**IES**, single-layer reflection tomography), which sits on the bottom and measures the seafloor-to-surface round-trip travel time. The measured travel time τ varies primarily due to changes in the heat content of the water column [18.42]. The recognition that heat content is well correlated with thermocline depth or dynamic height across the thermocline led to the use of τ to predict these variables for dynamics studies [18.43]. Arrays of **IES**s can be used to determine horizontal variations of geopotential height anomaly derived from the specific volume anomaly profiles; from these full-water-column (first mode) baroclinic shear profiles relative to zero velocity at the bottom can be calculated. The accuracy of this approach, compared to direct current observations, is excellent [18.44]. Further, a statistical regression technique has recently been developed based on the *gravest empirical mode* (**GEM**) [18.45]. In ocean regions with stable T - S relationships (most of the world's oceans) and where there is a dominant gravest vertical mode of low-frequency variability (most of the non-equatorial oceans), τ can be combined with information on the vertical structure of the water column (the **GEM**, derived from **CTD** profiles) to yield time series of full-water-column profiles of tempera-

ture, salinity, and specific-volume anomaly. The limit of how much independent information can be obtained from one observable, though, must be recognized.

The major source of *noise* for large-scale tomography experiments are sound speed (temperature) fluctuations caused by internal waves. There are ongoing efforts to invert this *signal* to obtain the parameters of internal wave models [18.46].

Inverting travel times in general for three-dimensional ocean temperature and velocity is an involved process that benefits greatly if it is done in the context of a data-assimilating numerical ocean circulation model. Data assimilation, starting with weather nowcasting and forecasting decades ago, is just coming into its stride in oceanography, using Kalman filtering and adjoint/variational techniques [18.47]. The assimilation of acoustic travel times directly into numerical ocean circulation models requires the specification of the measurement functional relating model parameters to the measured travel times. Only recently have data-assimilating ocean models had the vertical resolution for the forward acoustic problem, the calculation of the travel-time path integral. The wider use and acceptance of tomography will depend on the data-assimilation community using the acoustic data.

18.4.3 Acoustic Correlation Techniques

When sound propagates through the ocean, the wave-front is affected by turbulent fluctuations in the sound speed field (caused by temperature, salinity, and water velocity fluctuations), producing amplitude and phase variations; this is acoustic scintillation. If there is a larger-scale current advecting these small-scale fluctuations through the sound field, the received sound field carries information about the mean current. By transmitting sound through the water volume of interest along two paths, and cross correlating the two received signals, one can obtain the mean current perpendicular to the two paths (Fig. 18.20). This inverse process assumes certain forms for the spectrum of the turbulent fluctuations, e.g., isotropic turbulence.

Figure 18.21 shows other possible geometries integrating the simple acoustic travel-time concepts mentioned above, using reciprocal transmissions and multiple transceivers to obtain mean flow shear, currents, and sound speed both perpendicularly and along the paths, and vorticity. With appropriate amplitude weighting of acoustic beams, one can determine some range dependence. Measurements have been made with these scenarios in tidal channels [18.48].

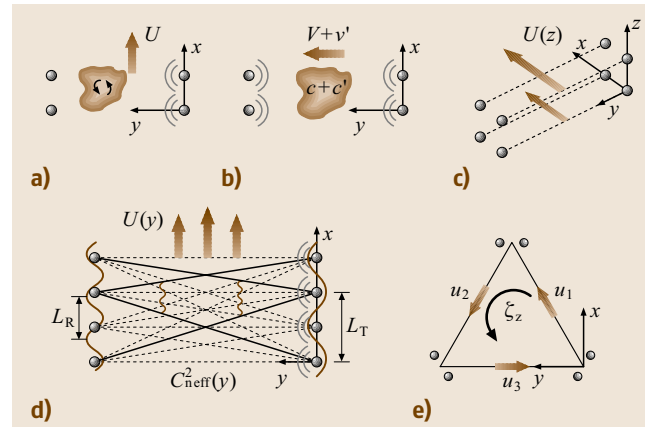


Fig. 18.21 (a) Parallel acoustic paths between two sources and two receivers. (b) Reciprocal transmission, where all transducers transmit and receive. (c) Two-dimensional arrays for shear and turbulent anisotropy measurements. (d) Linear arrays for spatial filtering of flow and turbulence parameters along the path. (e) Triangular array with paired transducers at each corner for horizontal velocity, turbulence, and vorticity measurements (courtesy of D. Di Iorio)

The acoustic scintillation flow meter (**ASFM**) has been commercialized (ASL Environmental Science). One version measures flow in hydroelectric dam pipes, and another measures flow in channels, e.g., the Second Narrows, Port of Vancouver. An **ASFM** system has been operating successfully in the Fraser River, on the British Columbia coast, since 1991.

18.4.4 Electromagnetic Sensing Using the Geomagnetic Field

The low-frequency (< 0.5 cycles per day) horizontal electric fields (HEFs) in the ocean are dominated by motional induction caused by the motion of conductive seawater through the Earth's permanent magnetic field. For the case of a flat-bottomed ocean with the length scale of the flow much larger than the water depth, a theoretical relationship between the HEF and the horizontal water velocity can be derived [18.49,50]; the motionally induced voltage E measured over a horizontal distance L caused by the ocean flow through the Earth's magnetic field B_z is (18.8)

$$E = V^* B_z L , \quad (18.11)$$

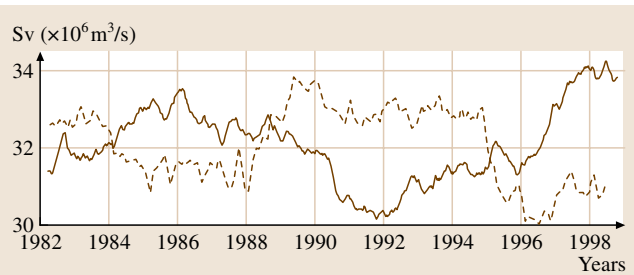


Fig. 18.22 Florida Strait transports (solid line in Sv) compared with the NAO (dashed line, rescaled and unitless [18.51])

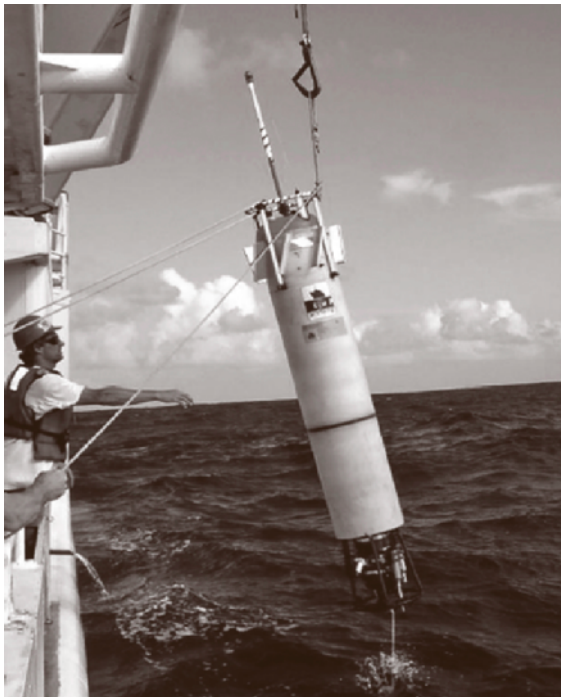


Fig. 18.23 Absolute velocity profiler (AVP); electrodes are in the black ring (courtesy of T. Sanford)

where V^* is the vertically averaged flow, weighted by the conductivity σ

$$V^* = \frac{\int (\sigma V) dz}{\int \sigma dz}. \quad (18.12)$$

To a first approximation V^* is the vertically averaged ocean velocity over the horizontal path L . The perturbation influence of mild and strong topography has also been considered.

If the conductivity profile is known from independent data, and if there is independent information about

the vertical shear of the horizontal currents, then the small conductivity bias is easily removed from the HEF-derived water velocities to yield the depth-averaged current – the transport, often called the barotropic velocity. Successful demonstrations of the theoretical relationship between HEFs and barotropic currents have been reported for point seafloor HEF measurements [18.52], for moving platforms [18.53], and for seafloor cables [18.54].

Fixed Sensors (Bottom Arrays, Cables)

Bottom instrument packages with two crossed electrode pairs with 6 m separation have been used to measure V^* and infer the barotropic velocity. A mid-latitude B_z of $36 \mu\text{T}$ and V^* of 1 cm/s (typical of mid-gyre open ocean) gives a voltage of $2 \mu\text{V}$. Even very stable silver-silver chloride electrodes drift much more than this; to overcome this drift, a water chopper switch is used to periodically reverse the polarity of the measurement. New designs are in progress to simplify the chopper. Given the simplicity and robustness of this method of measuring the barotropic flow, it will likely be used more in new long-term ocean observatories.

Many submarine cables have and are being used to measure the motionally induced voltages generated by water flow. An example of a short cable is the one crossing the Ria de Aveiro lagoon in Portugal, where a large tidal flow occurs [18.55]. The cable crossing the lagoon is 280 m long, so the measured (tidal peak) value of $E = 10 \text{ mV}$ gives a $V^* = 1.0 \text{ m/s}$ (using the value of B_z above). Combining this with the average depth of 15 m gives a flow rate or transport of $4 \times 10^{10} \text{ m}^3/\text{s}$. When tidal signals are removed, the weaker, residual flows are relevant in studying seasonal variations caused by river run-off, wind-forced currents, etc.

One of the first demonstrated links between ocean circulation and a climatic index, aside from the El Niño/Southern Oscillation, is provided by what may be the longest time series of ocean transport in existence. Measurements of the horizontal electric potential across the Florida Straits are directly related to the volume transport of the Florida Current; they were initiated in 1969 and have been measured since 1981 on inactive and powered submarine telecommunications cables, with calibration factors of 41 and 67 mV S/v and estimated uncertainties of 0.7 and 1.9 Sv , respectively ($1 \text{ Sverdrup} = 10^6 \text{ m}^3/\text{s}$). This long effort has demonstrated a significant relationship (correlation $R = 0.75$ at 95% CI) between the transport of the Florida Current and an index of short-term climate variability over the North Atlantic called the North Atlantic Oscilla-

tion (Fig. 18.22; [18.51]). Only such long records of spatially averaged quantities are suitable for statistical analysis.

Cable voltages are monitored around the world on an opportunistic basis using retired submarine telecommunications cables. The reader is referred to the most recent proceedings of the quadrennial conferences on scientific uses of submarine cables [18.56].

Moving Sensors

When the measurement electrodes are moving through the water at velocity V , then the measured voltage is

$$E = (V - V^*)B_z L. \quad (18.13)$$

For the case of electrodes towed behind a ship, often called the geomagnetic electro-kinetograph (GEK), near-surface currents can be measured. Two electrodes, one behind the other in the tow direction, measure velocity perpendicular to path. With accurate ship navigation (and velocity), the absolute V^* can be obtained [18.57]. This technique, though known for a long time, is little used.

Free-falling probes are often used to obtain vertical profiles of velocity, especially for turbulence and fine structure measurements where no vibration is permissible, (Fig. 18.23). An ADCP on the nose measures water velocity, with an absolute velocity reference provided by the fixed bottom, sensed by the ADCP.

18.4.5 Surface Current Mapping Using Radar Backscatter

Radar backscatter measurements over the ocean in the 1950s showed obvious Doppler shifts [18.58, 59] (see references in a recent review [18.60]). Under Bragg scattering conditions, surface waves with a length half that of the radio waves constructively reflect energy, in a manner analogous to X-ray diffraction from atoms in a crystal lattice. The frequency shift relative to the carrier in the absence of a current is

$$f = \pm \sqrt{(g/\pi\lambda)}, \quad (18.14)$$

where λ is the radio wavelength and is related to the advancing and receding phase velocity of the surface waves. A mean current displaces both of the corresponding peaks in the frequency spectrum by an amount equal to the associated Doppler shift. In this case the waves act as strongly reflecting passive tracers that produce a Doppler shift. The radar antenna beam pattern is usually such that a number of azimuthal beams are formed. The radar signal returns are range-gated, so that radial velocity is obtained as a function of the azimuth angle. With two or more radar stations horizontally offset providing geometrically independent data sets, a vector map of velocity can be formed. High-frequency (HF) radars of 3–30 MHz, and more commonly 12–25 MHz (25–12 m wavelength), are used. The lower frequencies can reach 200 km ranges with range bins of 5–10 km, while the higher frequencies reach 50 km with range bins of 1–3 km.

The current this method senses is not just the surface current but some average of the current in the upper water column because of the interaction between the exponentially decaying surface gravity wave orbital velocities

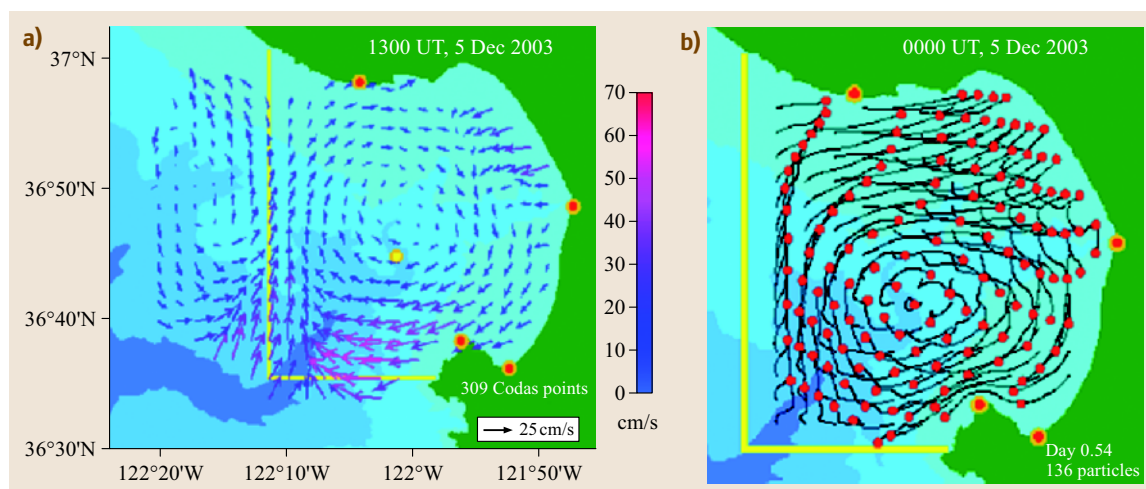


Fig. 18.24a,b HF radar surface currents (a) and particle trajectories (b) for Monterey Bay, California

and the vertical profile of the current. The weighting factor is $\exp(-2kz)$, the attenuation of wave orbital velocity with depth. For various reasonable, assumed current profiles (influenced by geostrophic currents, mixed layer processes, and Stokes drift), the sampling depths are all less than about one meter, but greater than an electromagnetic skin depth of a few centimeters. It may be possible to use different frequency radars (sensitive to different surface waves and their depth sampling) to extract depth-dependent velocity information. In the future it is not unreasonable to expect accuracies to drop from the present ≈ 10 cm/s to 2–5 cm/s, the typical precision due to the frequency resolution of the Doppler spectrum, given further instrument development and verification.

Figure 18.24 shows recent measurements made in Monterey Bay, California, based on data from a four-site HF radar network. Data from these systems are processed in real time. A normal-mode analysis mapping of the raw data makes it possible to produce continuously updated surface particle trajectories. Currents, particularly during the summer months, are now known to be driven in nearly equal proportions by eddies and upwelling filaments, sea breeze winds, and tidal fluctuations. The two-dimensional current maps available from the HF radar network make it possible to observe and separate the effects of these multiple driving forces.

Recent measurements such as these have led to much broader acceptance of radar data within the oceanographic community (see the collection of articles [18.61]). As of 2004, there are approximately 100 active antennae sites in the US, most funded for research. A contiguous HF radar system spanning the east coast of the US has recently been demonstrated. HF radar will likely be one of the first components of the nascent operational coastal observing systems.

18.4.6 Satellites

Besides the intrinsic value of their data products, satellite observations are of use to oceanographers to provide an additional context for their in situ measurements (Sect. 17.4). Several satellites relevant to oceanography research are described here.

The first oceanographic satellite was Seasat, launched in 1978. While it operated for only 105 days, it demonstrated many of the sensing modalities of subsequent satellites: radar altimetry to measure sea surface height, microwave scatterometry to measure wind speed and direction, scanning multichannel microwave radiometry to measure the sea surface temperature, visible and infrared radiometry to identify cloud, land, and

water features, and synthetic aperture radar (**SAR**) to observe the global surface wave field and polar sea-ice conditions. Seasat launched an entirely new mode of oceanography, one that for the first time had a global perspective.

The topography experiment (**TOPEX**)/Poseidon and Jason-2 altimeters measure sea surface height to an accuracy of ± 4 cm with a 10 day repeat cycle, nominal equatorial track spacing of 315 km, and an orbital period of ≈ 2 h. This allows the mapping changes in surface geostrophic currents as well as (time invariant) seafloor topography (seamounts affect local gravity and thus the sea surface height). The Gulf Stream, for example, has a 1 m sea surface height difference across it; a typical mesoscale eddy yields a 10 cm signal. The accuracy is a true tour de force, given that the total range is 1300 km (3 parts in 10^8).

Scatterometers today provide most of the operational observations of ocean wind speed and direction. Because the area and amplitude of centimeter-wavelength surface (capillary) waves is a function of wind speed, radar backscattering at the same wavelengths can be used to infer wind speed; by observing at different angles, the wind direction can be inferred. QuikScat, launched in 1999, maps out a 1800 km swath during each orbit and provides $\approx 90\%$ coverage of the ocean each day. Estimated accuracy is ± 1 m/s with a wind-vector resolution of 25 km.

Sea surface temperature has been determined since 1978 using the US National Oceanic and Atmospheric Administration (NOAA) polar-orbiting advanced very high-resolution radiometer (**AVHRR**). The instrument uses a scanning mirror/telescope to obtain a 2700 km-wide swath and views the Earth roughly twice a day. Absolute accuracy of $\pm 0.5^\circ\text{C}$ is obtained when compared with in situ data (such as from ships and buoys). Due to the eruption of Mt. Pinatubo in 1991 and an increase of aerosols in the atmosphere, modifications had to be made to the original algorithm; this was determined only years after the eruption. The inconsistency in the data was a significant problem in understanding global climate change. The recently deployed moderate-resolution imaging spectroradiometer (**MODIS**) on the Terra and Aqua satellites is an optical scanner that views the Earth in 36 channels with spatial resolution ranging from 250 m to 1 km; several of these channels overlap directly with the **AVHRR** channels.

The tropical rainfall measuring mission, launched in 1997, uses a precipitation radar with a horizontal resolution at the ground of about 4 km and a swath width of 220 km. It provides vertical profiles (250 m resolution

for vertical viewing) of rain and snow from the surface up to a height of about 20 km, detecting rain rates down to about 0.7 mm/h. At intense rain rates, where the attenuation effects can be strong, new data-processing methods have been developed that help correct for this effect.

Aquarius is a planned National Aeronautics and Space Administration (NASA) mission (\approx 2009) to measure sea surface salinity. The basis of the measurement is the dependence of the dielectric constant of seawa-

ter on salinity at microwave frequencies. The dielectric constant determines the surface emissivity, and this determines the brightness temperature, the measurable parameter. The baseline mission with an 8 day repeat cycle with a 350 km swath would provide 100 km resolution with an accuracy of 0.2 psu when averaged over a month. This will permit a reliable seasonal cycle to be measured.

18.5 Measurement Systems

Much of the challenge in oceanography is fielding the instrumentation; to reduce *delivery costs* it is usually the case that multiple sensors are combined into a suite of sensors supporting a common measurement objective. Here several examples are given: expendable sensors, a fixed bottom instrument package, a towed one, and several mobile platforms. In oceanography, there is always a tension between expendable, low-cost, low-accuracy probes and more-permanent, high-cost, and accurate sensor packages. Lastly, a description of the cabled, general-purpose long-term ecosystem observatory (LEO-15) is given; this example illustrates a trend to long-term sustained observations.

18.5.1 Expendable Sensors

In the early days of modern oceanography (World War II until the 1960s), bathythermographs (BTs) were deployed to 300 m from underway ships to measure temperature profiles (to obtain sound speed for anti-submarine warfare). In a small torpedo-shaped tow fish, a U-shaped xylene-filled copper tube swung an arm with a stylus across a glass slide coated with a thin layer of gold. Being somewhat awkward and limited in capability, these were replaced by expendable bathythermographs (XBTs). These similarly shaped devices contain a thermistor in the heavy lead nose and a spool of very fine, two-conductor wire in the tail. A corresponding spool of wire in the deck portion of the system assures no tension is on the wire. These free-falling probes can reach 1800 m, and cost about \$50 each. Accuracy is \approx 0.1 °C and depth is determined from a fall rate equation. There are now expendable sound velocimeters, CTDs, and (electromagnetic) current meters (more expensive); all are deployable from aircraft also.

18.5.2 HPIES

With the advent of sustained long-term ocean observatories, it will be important to choose sensors for their proven oceanographic utility, their resistance to degradation, and their ability to measure oceanographic variables remotely (an advantage that enhances reliability). An HPIES sensor suite combines a horizontal electrometer (HEM), a bottom pressure sensor, and an inverted echosounder measuring seafloor-to-sea surface acoustic travel time (Fig. 18.25). These measurements are integrating variables [18.62] because they are dominated by the currents and thermal variability with the largest vertical scales (and sometimes the largest horizontal scales). As such, these variables are ideal for observing the meso- to gyre-scale variations of the ocean circulation that are most likely related to climate change.

Arrays of IESSs yield four-dimensional views (x , y , z , and t) of water properties and low-frequency (< 0.5 cycle per day) baroclinic (depth-dependent) current shear. Arrays of HEMs yield three-dimensional views (x , y , and t) of conductivity-weighted barotropic



Fig. 18.25 A pressure inverted echosounder unit (PIES, courtesy of D. R. Watts)

velocity. The **HEM-IES** combination is greater than the sum of the parts, because it yields four-dimensional views of absolute water velocity. The accuracy of the derived absolute velocities has been demonstrated in an experiment in the Sub-Antarctic Front. Like the horizontal electric field variations, low-frequency pressure variations are related to an integral (in this case, horizontal) of water velocity fluctuations, and it can be argued from geostrophy that bottom pressure will be more sensitive to, if not dominated by, the motions with largest horizontal scales. As such, bottom pressure is a good partner with **IES** and **HEM** arrays, and thus HPIES. Among other applications, bottom pressure has been employed in studies of the variability of strong frontal currents (e.g., the Gulf Stream [18.63] and the Antarctic Circumpolar Current [18.64]), and studies of the kinematics and dynamics of atmospherically forced barotropic variability [18.65]. The combination of bottom pressure and two-component barotropic velocity gives the energy flux vector, useful in any dynamical context, as well as being a substantial improvement over the single pressure sensors presently used for tsunami detection.

In the future, **IES** acoustic transceiver arrays can also be used in a tomographic mode, precisely measuring travel times along acoustic ray paths between nodes. Given typical sound speed profiles one can expect at least surface reflected rays connecting bottom instruments up to a separation of 50 km in the deep ocean. With an array the number of paths grows quadratically. The travel time data can be inverted to produce the horizontal fields of temperature, velocity, and vorticity, complementing the more-local **IES**, **HEF**, and bottom pressure measurements. Higher-order statistics of the acoustic signals can be inverted to produce internal wave parameters (e.g., travel-time variance and internal wave strength).

18.5.3 Moored Profiler

Fixed sensors alone cannot provide all the required sampling; nor can any single sensing system. The moored profiler (Fig. 18.26) is one new tool that offers a vast improvement over fixed-depth sensors. By crawling up and down a standard mooring wire, it measures time series of temperature, salinity, and velocity profiles. Measuring entire profiles instead of a handful of discrete depths enables calculation of shear, strain, and turbulent dissipation (from overturns and shear parameterizations), while covering the entire water column. The system has been deployed in over 20 experiments with successes far outnumbering failures; the number of present and planned deployments indicates its reliability.

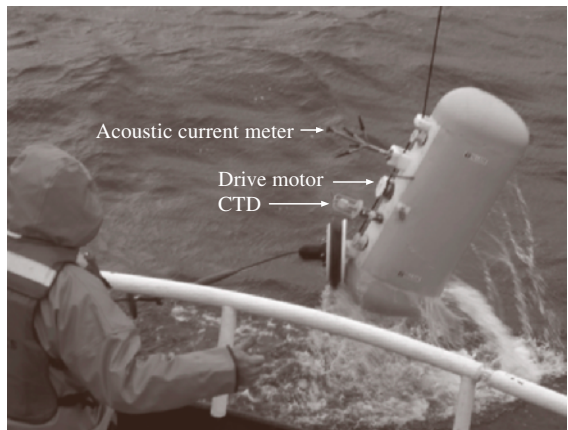


Fig. 18.26 A McLane moored profiler being recovered in the Puget Sound (courtesy of M. Alford)

Moored profilers have already resulted in substantial scientific advances in our understanding of variability in the eastern Atlantic, internal tides and mixing near Hawaii [18.66] and on the Virginia continental slope, the variability of the Kuroshio extension [18.67], and the evolution of arctic thermohaline layers and double-diffusive layers in the Barbados staircase. Future developments to the platform will likely include increasing profiling speed from 0.25 m/s to 0.4 m/s to reduce tidal aliasing, adding payload capability (e.g., more sensors), and providing docking to external power and communications (either via a seafloor cabled observatory system or a large battery pack and acoustic modem, for instance).

18.5.4 TriSoarus Towed Vehicle



Fig. 18.27 Trisoarus towed undulating vehicle (courtesy of C. Lee)

TriSoarus is a towed, undulating vehicle for high-resolution, three-dimensional surveys of the upper ocean. TriSoarus began life as a SeaSoar vehicle, but has been heavily modified to increase profiling range on unfaired cable. Large symmetric foil section wings and a gravity-driven roll-stabilizing aileron significantly enhance range and stability compared to a stock SeaSoar. The actuator and telemetry system have been upgraded by adapting Triaxus components (another *box-kite* towed vehicle). Thus, the two vehicles have identical subsea and topside electronics suites, down to the software control algorithm. Instrument payloads are similar. TriSoarus provides flexible support for a wide range of payloads, including physical, optical, biological and chemical sensors, and the system has been designed to ease the integration of new instruments. The basic sensor suite includes a CTD, chlorophyll fluorometer, transmissometer and dissolved oxygen sensor, with a fiber-optic tow cable providing high-bandwidth telemetry. At a typical tow speed of 8 knots, the vehicle profiles from the surface to 200 m, providing along-track resolutions of 2 km or better.

The TriSoarus has been used in the Adriatic Sea to measure the response to three primary driving forces:

1. wintertime Bora winds
2. weaker, along-basin Sirocco winds
3. seasonal buoyancy input from the Po River and other sources;

all govern the evolution of coastal filaments, eddies, and fronts in the northern Adriatic.

18.5.5 Turbulence and Small-Scale Structure

Seawater density is determined primarily by temperature and salinity, and the different molecular properties of these two scalars give rise to many interesting phenomena. Differential diffusion of heat and salt has the potential to radically alter large-scale ocean circulation due to freshwater mixing in polar regions. These phenomena are also important in estuaries where salt stratification is crucial to mixing. Anywhere there is warm salty water below cold fresh water, double-diffusive salt fingering can occur.

To study such phenomena, the MARLIN towed vehicle carries a fast salinity probe, which resolves conductivity and temperature on sub-centimeter scales (Fig. 18.28). Hundreds of kilometers of salinity data were obtained from MARLIN in 2002 during the Hawaii ocean mixing experiment (Sect. 18.6.1 below).

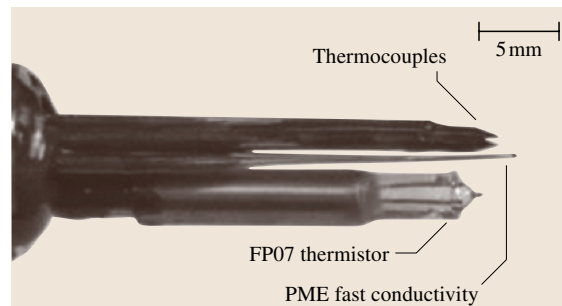


Fig. 18.28 The MARLIN fast salinity probe (courtesy of J. Nash)

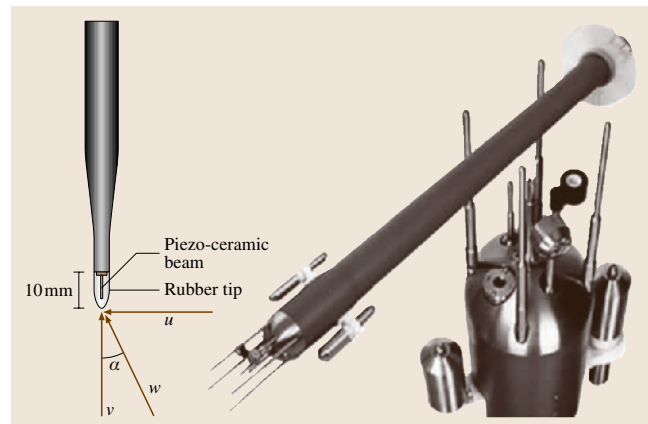


Fig. 18.29 Shear probe and microstructure profiler (Alec Electronics, Kobe)

Turbulence measurements must be made on platforms that are free of vibration; this has driven the development of free-falling microstructure measurement platforms. Turbulent velocity fluctuations are measured with a shear probe (Fig. 18.29), which is the standard sensor for turbulence measurements. The probe's sensing element consists of a parabolically shaped, axially symmetric flexible rubber tip. For small angles of attack, the oncoming flow with velocity W produces a hydrodynamic lift force proportional to the cross-stream velocity component. A piezoceramic beam, located at the center of the rubber tip, translates the lift force into an electrical signal. Differentiating this produces a signal proportional to the rate of change of cross-stream velocity du/dt . Under Taylor's frozen-field assumption, the velocity shear is then $du/dz = W du/dt$.

18.5.6 Floats



Fig. 18.30 Four MLF2s ready for Hurricane Isidore after Puget Sound testing in July 2002 (courtesy of E. D'Asaro)

Float platforms are increasingly used to carry a payload of diverse sensors dependent on the application. A recent float developed at the Applied Physics Laboratory is the mixed layer float-2 (MLF2, (Fig. 18.30)). Earlier experience showed that, although much could be learned from temperature and pressure measurements, these alone were insufficient to diagnose the dynamics of oceanic turbulent boundary layers. Measurements of shear, stratification, and surface waves are necessary. Furthermore, accurate ballasting of the floats under conditions of strong mixing in general requires knowledge

of the density of the seawater, so salinity measurements were needed. Also, there is a great potential for studying biological phenomena using optical sensors. Finally, advances in satellite communications offered two-way data transmission so that floats can be controlled and their mission parameters modified remotely. These factors dictated the construction of a larger float with sufficient power (a larger battery pack; solar cells for duration) and the capability of easily accommodating a variety of sensors.

MLF2 displaces 50L and has the ability to surface repeatedly by controlling 750 cm³ of active volume control with an extruding piston. It has a cloth drogue, but this can be folded and unfolded as many times as desired. The MLF2 mission consists of periods of Lagrangian drift typically 12 h long. Between these the float surfaces, uses GPS to determine its position, and transmits its position and some of its data using Iridium. It then waits for instructions before beginning another drift period.

The float can carry a large instrument suite, including a Doppler SONAR, altimeter, CTDs, accelerometers, a photosynthetic active radiation (PAR) sensor, fluorometer, and horizontal electric field sensors. MLF2 has been used in a study of the wintertime North Pacific mixed layer in 2000 and in studies of upwelling off Oregon in 2000 and 2001. An air-deployment package was used to deploy MLF2s into hurricanes during 2002–2004.

The sensors allow much better understanding of the behavior and accuracy of floats. For example, in a strat-

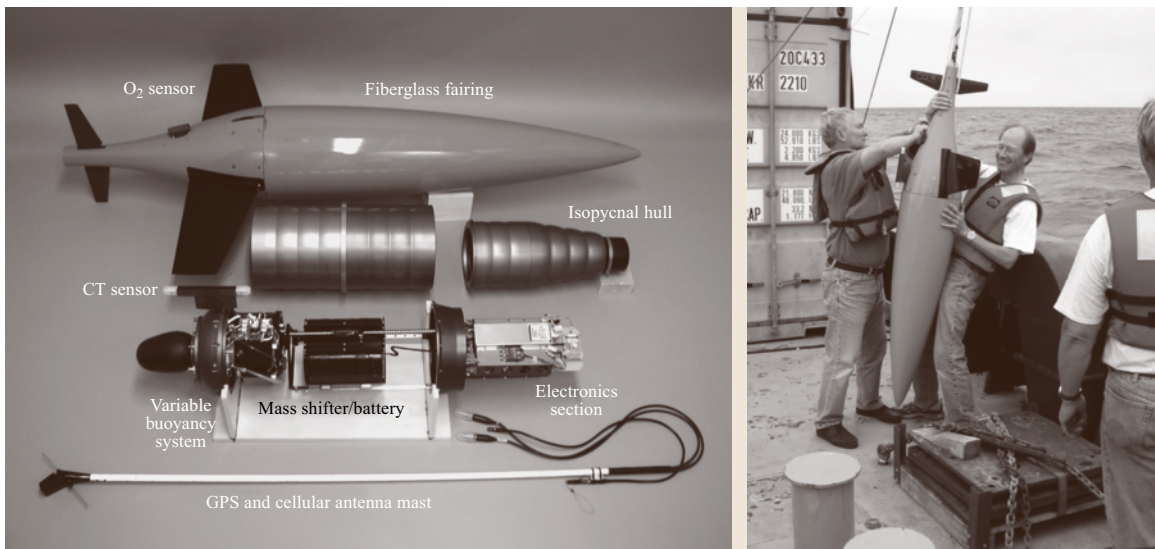


Fig. 18.31 Seaglider: (left) components and (right) being deployed in 2004 in the north Pacific

ified fluid, the dominant cause of drag on the float is the radiation of internal waves. This internal wave drag is much larger than the normal form drag at low speeds and causes the floats to be Lagrangian for frequencies higher than about $N_B/30$, where N_B is the buoyancy frequency. Because most mixing events in a stratified fluid happen on time scales of about N_B , this means that floats can be good instruments to measure mixing rates in the ocean interior. These results are described in a recent paper [18.68].

18.5.7 Gliders

Gliders are autonomous mobile platforms that use changes in buoyancy combined with wings to provide a horizontal motive force. As with Argo and other floats, oil is pumped in and out of an external bladder to effect the buoyancy change. There are three presently produced: the Spray (Scripps Institution of Oceanography), the Slocum (Webb Research Corp.), and the Seaglider (University of Washington) (Fig. 18.31); many variants are in progress. Gliders fill a niche between floats and powered vehicles, providing a directed platform with long duration.

The Seaglider [18.69] changes its attitude by mechanically shifting its battery pack fore and aft and side to side. When it surfaces, a combined GPS/Iridium antenna extends about one meter above the water. GPS provides position and time synchronization. Iridium provides real-time 2400 baud two-way communications; missions are routinely controlled from shore and new software can be uploaded. Typical sensors are temperature, conductivity, pressure, and dissolved oxygen. Because buoyancy/volume and drag are significant issues, interfacing new sensors is nontrivial.

Figure 18.31b shows a Seaglider in the process of being launched from an oceanographic vessel for a cross-Pacific mission that lasted 6 months, made 600 dives and covered 3 Mm at 1/2 kt using an average of 1/2 W. This particular glider carries a RAFOS acoustic receiver; ranges to 1900 km were obtained.

18.5.8 Autonomous Undersea Vehicles (AUVs)

AUVs are now used for short-duration (typically 1 day at 3 kt) missions, carrying a variety of sensors ranging from simple CTDs to very sophisticated bottom mapping SONARs. An example of a small one (19 cm diameter, 160 cm long, 37 kg) is the REMUS (remote environmental monitoring units) vehicle (Fig. 18.32). A standard



Fig. 18.32 REMUS AUV (Hydroid, Pocasset)

configuration carries a small up- and down-looking ADCP, CTD, sidescan SONAR, and light-scattering sensors; other sensors that have been used (not all at once) include an acoustic Doppler velocimeter, a shear probe, a plankton pump, up and down looking radiometers, a DIDSON (dual frequency identification sonar) acoustic lens, GPS, and deployable acoustic navigation transponders. These are still rather expensive (250 000 US\$) and require skilled technical support. Two other vehicles are the autonomous benthic explorer (ABE, Woods Hole Oceanographic Institution) intended for deep use around topography (e.g., measuring vertical heat flux above hot vent fields), and the Dorado (Monterey Bay Aquarium Research Institute), a large (21 in-diameter) vehicle that has been used under the ice in the Arctic. The latter application will likely be a major driver for AUVs and gliders, as a means of directed sampling. The military is a major driver behind glider and AUV development.

18.5.9 LEO-15

The long-term ecosystem observatory (LEO) off the US New Jersey coast (Fig. 18.33) is a forerunner of ocean observing systems of the future. The core is a cabled node in 15 m of water, installed in 1996. Many in situ sensors and platforms are connected to this central core: winched CTD, ADCP, benthic acoustic stress sensor (BASS) tripod, electromagnetic current meter, optical backscatter, wave height and period, temperature, and fluorescence, video cameras, optical profiling node with chlorophyll, dissolved organic matter, fluorescence, spectral light backscatter, and particle size, and a REMUS AUV docking station. Around it are many autonomous instruments (some on land): moorings with temperature, salinity, and current sensors, IMET (improved meteorological) meteorological buoy, HF radar buoy extending the range of the shore-based system, hy-

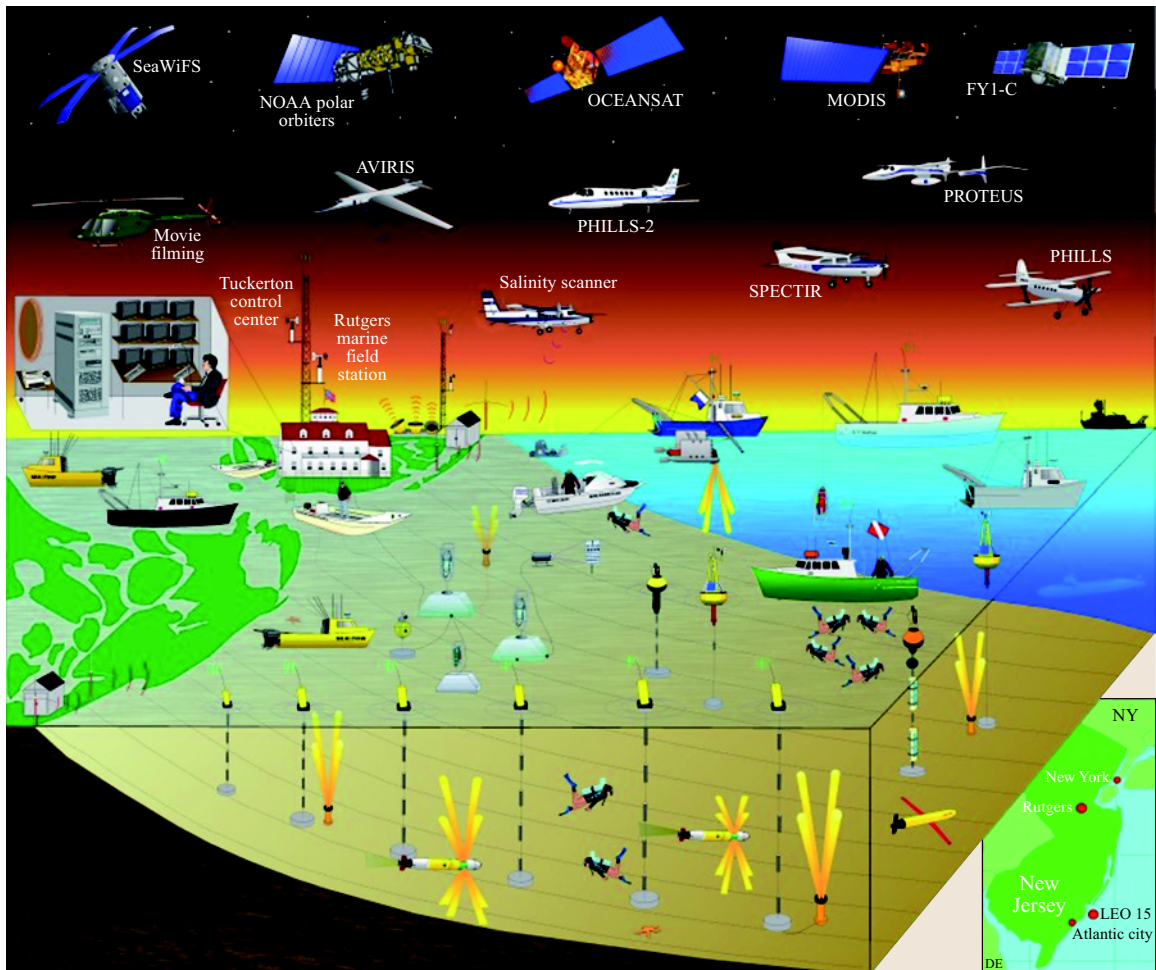


Fig. 18.33 Long-term ecosystem observatory (LEO-15) instrumentation used for the 2000–2001 experiment (courtesy of O. Schofield and S. Glenn)

perspectral radiometers to provide ground truth for new satellite sensors, gliders and AUVs, land IMET sensors, and SODAR for wind profiles (Chap. 17). These sensor systems are complemented by ships, aircraft, and satellites.

To date, the complex sampling shown in the figure can only be sustained for one or two months at a time.

A major goal of this integrated ocean observatory is to develop a real-time capability for rapid environmental assessment and physical and biological forecasting in coastal waters. To this end, observational data from all sources are collected in real time, permitting adaptive sampling of episodic events and assimilation into ocean forecast models. This measurement-rich situation provides a unique opportunity to refine and verify models.

18.6 Experiment Case Studies

Actual oceanographic field experiments are usually expensive and often last a number of years, with analysis taking a decade or more. There is always a variety of

measurements made using diverse technologies that facilitate novel approaches to the science questions. Two cases illustrate the complexity.

18.6.1 Hawaii Ocean Mixing Experiment (HOME)

The ocean's steady-state thermohaline structure is determined by downward diffusion balanced against upward currents. An outstanding oceanographic problem is that independent measurements of the ocean's vertical temperature structure and the amount of turbulent mixing are not consistent. Measurements find approximately one tenth of the mixing necessary to agree with the warm temperatures detected in the ocean's depth. A long-standing suggestion is that mixing does not occur uniformly over the entire ocean, but is concentrated in the vicinity of rough topography (Sect. 18.3.3). The Hawaii ocean-mixing experiment (HOME) has been an effort to test this theory with observations and

computational models of mixing along the Hawaiian Ridge [18.70].

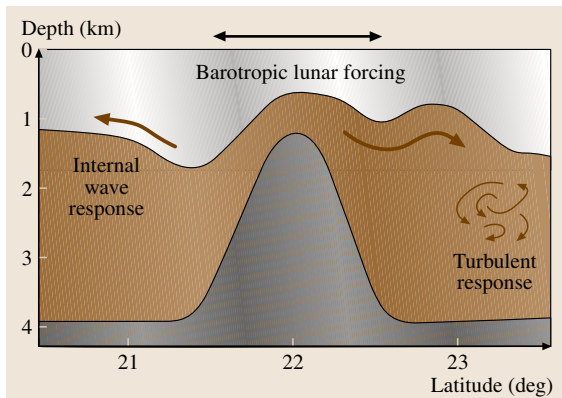


Fig. 18.33 Schematic of energy cascade near abrupt topography like the Hawaiian Ridge

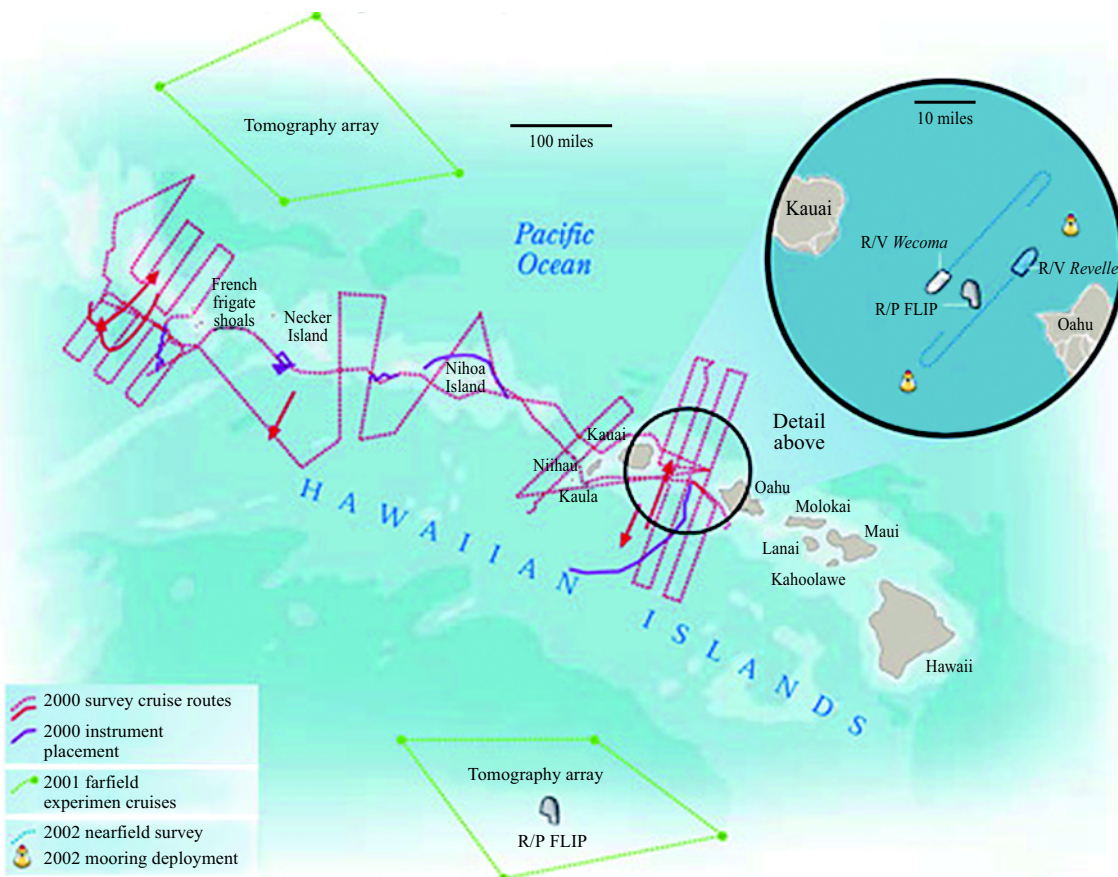


Fig. 18.34 HOME field program

The Hawaiian Ridge is an attractive place for a mixing experiment because the topography is steep and energy is available for mixing in the form of tides, which strike the ridge perpendicularly (Fig. 18.33). Recent inferences from satellite altimeter data suggest that half of the 2 TW required for ocean mixing can be derived from the tides. Mixing is envisioned as a cascade from barotropic surface tides, through baroclinic internal tides and breaking internal waves, to turbulence.

Observing the tides-to-turbulence cascade in the ocean is a considerable challenge. Spatial scales range from megameters (the size of ocean basins and major topographic features) down to centimeter scales, where molecular diffusion occurs. The HOME project used an integrated program of modeling and observation; the latter includes components to survey the entire ridge, as well as to study far- and near-field regimes (Fig. 18.34). The numerical modeling of surface and internal tides and the analysis of historical data completed the experimental approach.

Two major challenges were to isolate baroclinic variability associated with the tides from a background of energetic processes and to extrapolate the results obtained from HOME to other regions of the ocean where the tides are an important energy source for open ocean mixing. In both regards, numerical models provide the means for interpretation of a comprehensive but undersampled set of observations, and data assimilation provides an optimal way to combine all available data into dynamically consistent estimates of barotropic and

baroclinic energy fluxes, and hence to constrain the amount of tidal energy available for localized mixing. Models can also be used to determine the topographic and oceanic conditions favorable for energetic tide-induced mixing, and thus experiment planning. Finally, models provide a dynamical context in which to synthesize and generalize the results, providing the opportunity to evaluate various turbulent closure schemes against direct and integrated measures of dissipation and diapycnal mixing.

Historical data from moored current meters, [CTDs](#), and [ADCPs](#) (collected for other purposes) were analyzed for the presence of signatures of fine-scale mixing activity, with the results being grouped according to depth, isopycnal, proximity to topography, or other environmental variables. This work helped to determine the locations and ubiquity of regions where strong mixing activity appears to be common irrespective of energy source and this has guided the subsequent deployment of field resources.

The survey component quantified the geographic variability of turbulent mixing (shear, stratification, and dissipation) in the vicinity of the Hawaiian Ridge. Five cruises in 2000 were conducted measuring temperature, salinity, horizontal and vertical velocity, turbulent energy dissipation, optical attenuation, acoustic backscatter, and seafloor topography. Horizontal resolution was as fine as $O(1\text{ m})$, with ranges of roughly 1000 km along the ridge and 100 km across the ridge. The finest vertical resolution was $O(1\text{ cm})$, ranging over the entire ocean depth. In an extensive survey along the 3000 m isobath, the absolute velocity profiler ([AVP](#), (Fig. 18.23)) was used to estimate the semidiurnal internal tide energy-flux radiating away from the ridge, confirming energy was originating at the ridge rather than passing through it. Other measurements were made using SeaSoar (measuring stratification and shear to 300 m), the advanced microstructure profiler ([AMP](#)), and towed body ([MARLIN](#), (Fig. 18.28)) capable of making measurements of turbulence and fine structure to depths of 3400 m, and moorings with [ADCPs](#) and other instrumentation. Model energy-flux hot and cold spots were consistent with these and other observations though with some differences in magnitude and direction.

The survey results guided the selection of sites for the near- and far-field components. The former included many of the same measurements as for the survey, concentrated on the Kaena Ridge, a representative mixing *hot spot*, on the northwest side of Oahu bordering the Kauai Channel. The far-field experiment consisted of tomographic arrays and pressure sensors and horizontal

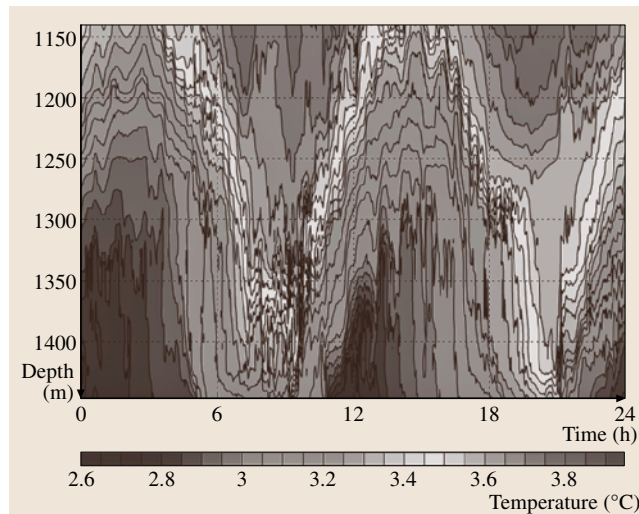


Fig. 18.35 Moored temperature as a function of depth and time in the eastern Kauai Channel near the Kaena Ridge [18.70]

electrometers on the north and south sides of the ridge. These were used to estimate the first two terms of the equation:

$$\begin{aligned} \text{Energy lost from the barotropic tide} \\ = (\text{baroclinic tide radiative energy}) \\ + (\text{local dissipation}). \end{aligned}$$

R/P FLIP (floating instrument platform) (Fig. 18.38) was included in both the near- and far-field components to obtain high-resolution vertical profiles and Doppler SONAR data.

In combination, these measurements provided striking evidence that energy is being transferred from the incident tide to internal waves that then break, giving rise to turbulence. This occurs mainly at local *hot spots*. A modest amount of energy radiates as baroclinic tides into the ocean interior; most appears to be dissipated locally. This conversion from the tides to turbulence represents a cascade of energy from the very large tidal scales of 1000 s of km, down to the relatively tiny scale of turbulent dissipation, approximately 1 cm. A mooring near the Kaena Ridge (Fig. 18.35) equipped with temperature (and other) sensors showed peak-to-peak internal wave

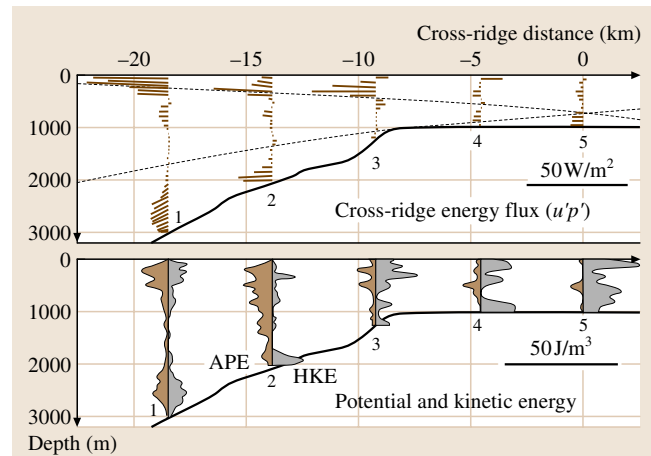


Fig. 18.36 Energy flux and potential and kinetic energy as a function of depth and range on the Kaena Ridge (courtesy of J. Nash et al.)

displacements of 300 m (compared with the 1 m surface tide) during spring tide at the semidiurnal period [18.70]. Baroclinic generation occurs over the steep upper flanks of the ridge and forms beams that propagate upward and downward. Superposition of waves from the northern

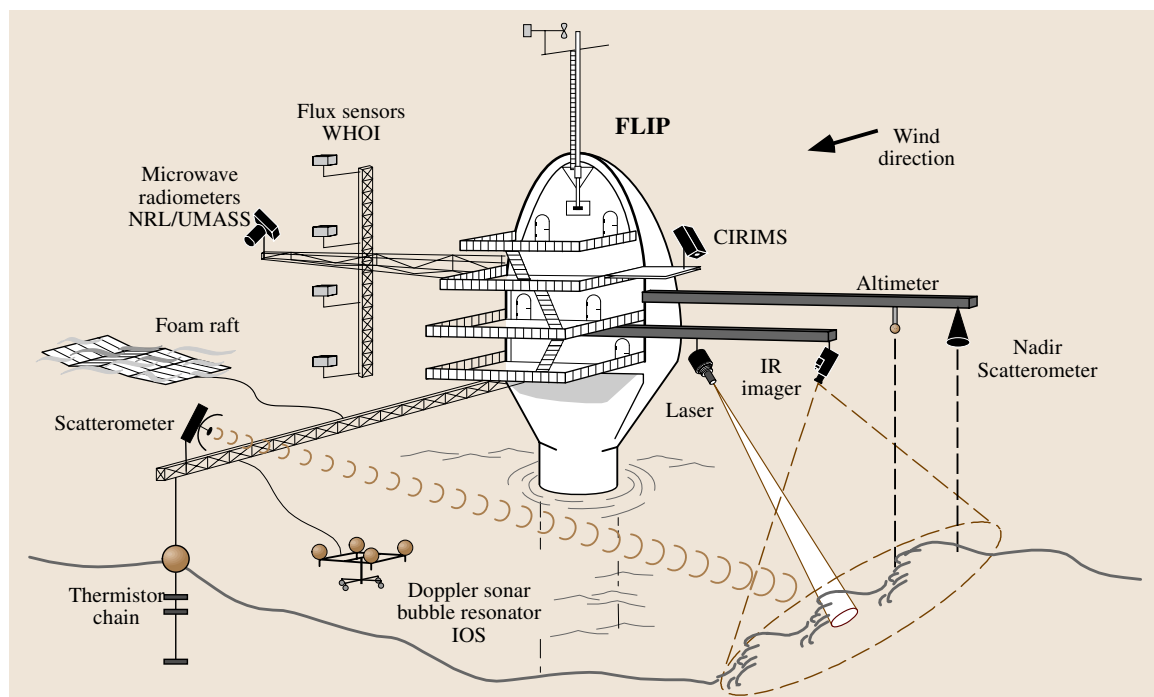


Fig. 18.37 FAIRS focused on coordinated measurements to improve understanding of air-sea interaction and its effects on remote sensing



Fig. 18.38 R/P FLIP drifted freely so the hull rotated to remain in the same orientation to the prevailing wind

and southern flanks of the ridge (and traveling in opposite directions) produce a standing-wave pattern over the ridge top. The standing wave has no net energy flux, but the interference of waves produces regions of high and low available potential energy-to-horizontal kinetic energy (**APE:HKE**) ratio that correspond to the ridge flanks (high APE) and ridge top (low APE) (Fig. 18.36).

18.6.2 Fluxes, Air–Sea Interaction, and Remote Sensing (FAIRS)

To better characterize and quantify the transfer of momentum, heat, and gas across the air–sea boundary, measurements of their underlying physical mechanisms were made using remote sensing instruments as part of the fluxes, air–sea interaction, and remote sensing (FAIRS) experiment (Fig. 18.37). This was a 32 day excursion aboard the research platform R/P FLIP off the coast of Monterey, California. FLIP is a unique 100 m vessel that is towed to sea and is literally flipped up on end so that only the top 20 m is above the water surface (Fig. 18.38). The result is a stable platform for housing scientists and their instruments, ideal for making air–sea interaction measurements because of its low flow distortion and high stability during rough conditions. The experiment has provided an extensive suite of complementary measurements that combine remote sensing, marine meteorology, and physical oceanography [18.71].

Microbreaking Waves and Infrared Imagery

The most obvious phenomena at the air–sea interface are ocean surface waves, especially large-scale breaking waves, or whitecaps. Less obvious is microscale wave breaking, or microbreaking, which occurs when small,



Fig. 18.39 FAIRS infrared sensors (courtesy of A. Jessup)

wind-generated waves about 10 cm to 1 m long gently break. These short, wind-driven waves increase to a height of a few centimeters until they become too steep to support themselves and consequently *break* and overturn the water right at the surface. This process transfers momentum into the upper ocean as turbulence and mixing that enhances the transfer of heat and gas between the ocean and atmosphere.

The remote sensing instruments mounted on the decks and booms of FLIP included an infrared imager, microwave radiometers, microwave radars, and video cameras. A passive technique used the infrared imager to take a picture of the ocean’s surface temperature, concentrating on the small but measurable temperature variations that occur when a breaking wave causes water from below to be mixed to the surface. An active technique used a CO₂ laser to heat a patch of water; the patch was then monitored by the imager to time its decay. During rough seas when the surface was broken frequently and repeatedly by microbreaking, the heated patch cooled down in less than a second. During very calm conditions, the patch remained visible in the infrared image for several seconds. This length of time for the heated patch to revert to the surrounding surface temperature is used to quantify the flux of heat at the surface as well as the amount of turbulent mixing.

Parasitic Capillary Waves and Microwave Backscatter

One characteristic of a microbreaking wave is that small capillary waves are generated on its forward face and travel along with the wave as it breaks. These capillary waves ride along on the steep front face of microbreakers, and thus they appear tilted with respect to the look angle of (microwave) radar; this tilting effect may explain why more reflected energy is observed than is

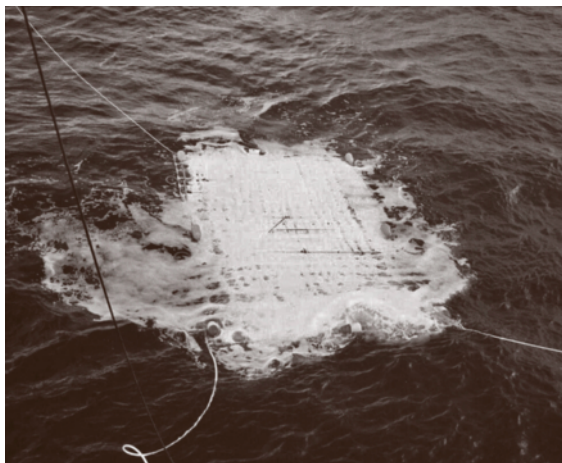


Fig. 18.40 Foam generator raft produces a steady foam by forcing air through a matrix of gas-permeable tubing

predicted by current models. By combining infrared and microwave techniques, the role of microbreaking in surface fluxes and radar backscatter can be better understood.

Whitecap Emissivity and Microwave Radiometry

Microwave radiometers are currently used to measure wind speed from satellites by exploiting the dependence of ocean surface emissivity on surface roughness. Because the wind direction signal is so small, the emissivity of foam generated by large-scale breaking waves becomes significant. To characterize the effect of foam on radiometer measurements, a 3×7 m raft made of gas-permeable tubing generated a uniform area of sea foam that filled the footprint of the microwave radiometer (Fig. 18.40); in this way a degree of *laboratory control* was brought to the field experiment. By measuring the microwave signal from the sea surface with and without foam, the foam's emissivity could be determined [18.72].

Surface Roughness and Air–Sea Fluxes

Over the ocean, direct measurements of turbulent air–sea fluxes are difficult due to platform motion, flow distortion, and the effects of sea spray. Instead, marine meteorologists have used flux–profile relationships that relate the turbulent fluxes of momentum, heat, and moisture (or mass) to the more easily measured profiles of velocity, temperature, and water vapor (or other gases), respectively (Sect. 17.2.1). These relationships are required for indirect methods such as the bulk

aerodynamic, profile, and inertial dissipation methods that estimate the fluxes from mean, profile, and high-frequency spectral measurements, respectively. The flux–profile or flux–gradient relationships are also used extensively in numerical models to provide lower boundary conditions to *close* the model by approximating higher-order terms from low-order variables. Direct covariance techniques, gradient techniques combined with Monin–Obukhov similarity theory, and inertial dissipation methods are all used to infer fluxes. However, the use of land-based measurements to infer ocean surface fluxes has been questioned, particularly close to the ocean surface where wave-induced forcing can affect the flow. Therefore, the applicability of Monin–Obukhov similarity theory to ocean–atmosphere surface layers is a current topic of research.

During FAIRS, micrometeorological flux measurements were used to improve the parameterizations of heat and momentum fluxes [18.73]. Direct measurement of the atmospheric fluxes along with profiles of water vapor and temperature were performed near the end of the 18 m port boom (Fig. 18.39). Turbulent fluxes of momentum, heat, and water vapor were measured by sonic anemometers, sonic thermometers, and infrared hygrometers, respectively. A mast supported a profiling system that moved a suite of sensors between 5 m and 15 m above the mean ocean surface. The moving sensors were referenced against a fixed suite of sensors to remove naturally occurring variability during the profiling periods. The measurements of heat and momentum flux, combined with infrared and microwave measurements, quantify the correlation of air–sea fluxes with surface roughness, ranging in scales from dominant gravity waves to capillary waves and microbreaking.

Sea-to-Air Dimethylsulfide Fluxes

One of the consequences of wave breaking and sea surface renewal is that soluble gases are transferred between the ocean and the atmosphere. Dimethylsulfide (DMS) plays an important role in atmospheric chemistry and climate through its oxidation to sulfuric acid and subsequent formation of cloud condensation nuclei. Although the disequilibrium can be measured fairly easily for most gases, direct measurements of the gas transfer velocity are quite difficult. However, if the transfer velocity for one gas is known, the transfer velocity for other gases can be fairly easily calculated.

DMS fluxes were measured using two different techniques, the gradient flux (GF) approach and relaxed eddy accumulation (REA). In the GF technique, air samples are obtained at different heights from the sur-

face, and the gradient is related to the gas flux through simultaneous micrometeorological measurements and Monin–Obukhov similarity theory. In the REA, two samples are taken at the same height, one when the vertical wind has a significant upward component and one when the vertical wind has a downward component; the flux is proportional to the concentration difference between the two samples and the variance in the vertical wind. The gas transfer results using both GF and REA were consistent with previous measurements, with the REA values being somewhat higher than those from GF [18.74]. This measurement provided an opportunity for one of very few *in situ* comparisons of different methods of gas transfer measurement, and the first one for DMS. Measurements of the concentration of DMS in surface seawater were also performed, allowing estimation of the gas transfer velocity and comparison to the heat transfer velocities measured using the active infrared technique described above.

Turbulent Velocity and Enhanced Dissipation

A unique surface-tracking float was used to link measurements of the turbulent velocity field beneath the surface to the signature of turbulence on the surface (Fig. 18.41). Subsurface acoustic sensors were used to examine the link between bubble size distributions and near-surface turbulence. The float supported three Doppler SONARs, two resonators and a thermistor and pressure sensor. The velocity profiles, resolved on the centimeter scale, yielded wavenumber spectra directly. Energy dissipation was inferred from the spectra, consistent with an inertial subrange. The bubble size distribution was measured with a resonator placed close to the acoustic Doppler profiler. Video recordings of the float allowed verification of wave breaking events and provided estimates of the size and propagation speed of whitecaps. In addition, the directional surface wave field was monitored with a suite of Doppler SONARs mounted on the hull of FLIP. Measurements of the thermal structure of the surface layer of the ocean were acquired with two chains of self-recording thermistors to a depth of 70 m.

References

- 18.1 W. Munk: *Oceanography Before, and after, the Advent of Satellites*, *Oceanography and Society*, ed. by D. Halpern (Elsevier, Amsterdam 2000) p.1
- 18.2 C. Wunsch: What is the thermohalocline circulation?, *Science* **298**, 1179–1180 (2002)
- 18.3 M. Eble, F. Gonzalez: Deep-ocean bottom pressure measurements in the northeast Pacific, *J. Atmos. Ocean. Tech.* **8**, 221–233 (1991)
- 18.4 I. Shkvorets, F. Johnson: *Proc. IEEE Oceans 2004 OT0'04 Conference* (Kobe, Japan 2004)



Fig. 18.41 A surface-following float provided subsurface measurements of turbulent velocity and bubbles generated by large-scale breaking waves

Simultaneous video recordings of wave breaking events during which turbulent velocity and bubble fields were measured show that turbulence and dissipation in the ocean surface layer is greatly enhanced due to wave breaking [18.75]. Dissipation rates associated with a breaking event are up to five orders of magnitude greater than background rates. Bubbles of all sizes are rapidly injected beneath breaking waves and decay slowly after approximately one wave period. The large velocities that occur during breaking are sufficient to counteract the rise in velocity of larger bubbles only briefly. However, the more-persistent turbulent velocity that remains after breaking may keep small bubbles in suspension for a significant time. These and other observations provide insight into the turbulent transport in the near-surface layer and the dissipation of wave energy; with these measurements it will be possible to determine if infrared techniques can be used (more simply) to estimate near-surface dissipation rates.

- 18.5** K. Mackenzie: Nine-term equation for sound speed in the oceans, *J. Acoust. Soc. Am.* **70**, 807–812 (1981)
- 18.6** G. Wong, S. Zhu: Speed of sound in seawater as a function of salinity, temperature, and pressure, *J. Acoust. Soc. Am.* **97**, 1732–1736 (1995)
- 18.7** H. Medwin: *Sounds in the Sea* (Cambridge University Press, Cambridge 2005)
- 18.8** J. Rizoli (Ed.): *Proc. IEEE/OES Seventh Working Conference on Current Measurement Technology, San Diego, California* (The Printing House, Stoughton 2003)
- 18.9** P. Collar: *A Review of Observational Techniques and Instruments for Current Measurement in the Open Sea, Report No. 304* (Institute of Oceanographic Sciences, Surrey 1993)
- 18.10** D. Frye, N. Hogg, C. Wunsch: A long duration mooring for ocean observation, *Sea Technol.* **45**, 29–39 (2004)
- 18.11** J. Ledwell, E. Montgomery, K. Polzin, L. St. Laurent, R. Schmitt, J. Toole: Evidence for enhanced mixing over rough topography in the abyssal ocean, *Nature* **403**, 179–182 (2000)
- 18.12** J. Ledwell, A. Watson, C. Law: Mixing of a tracer in the pycnocline, *J. Geophys. Res.* **103**, 21499–21529 (1998)
- 18.13** K. Polzin, J. Toole, J. Ledwell, R. Schmitt: Spatial variability of turbulent mixing in the abyssal ocean, *Science* **276**, 93–96 (1997)
- 18.14** A. Watson, J. Ledwell, S. Sutherland: The Santa Monica Basin tracer experiment: Comparison of release methods and performance of perfluorodecalin and sulfur hexafluoride, *J. Geophys. Res.* **96**, 8719–8725 (1991)
- 18.15** W. Sturges, T. Wallington, M. Hurley, K. Shine, K. Sihra, A. Engel, D. Oram, S. Penkett, R. Mulvaney, C. Brenninkmeijer: A potent greenhouse gas identified in the atmosphere: SF₅CF₃, *Science* **289**, 611–613 (2000)
- 18.16** J. Ledwell, K. Polzin, L. St. Laurent, R. Schmitt, J. Toole: Evidence for enhanced mixing over rough topography in the abyssal ocean, *Nature* **403**, 179–182 (2000)
- 18.17** M. Sundermeyer, J. Ledwell: Lateral dispersion over the continental shelf: Analysis of dye-release experiments, *J. Geophys. Res.* **106**, 9603–9621 (2001)
- 18.18** F. Rowe, J. Young: *An ocean current profiler using Doppler sonar, IEEE Proc. Oceans 79*, 292–297 (IEEE Proc. Oceans, New York 1979)
- 18.19** R. Pinkel: Observation of strongly nonlinear motion in the open sea using a range-gated Doppler sonar, *J. Phys. Oceanogr.* **9**, 675–686 (1979)
- 18.20** C. Wilson, E. Firing: Sunrise swimmers bias acoustic Doppler current profiles, *Deep Sea Res. Part 39*, 885–892 (1992)
- 18.21** R. Pinkel, J. Smith: Repeat sequence coding for improved precision of Doppler sonar and sodar, *J. Atmos. Ocean. Technol.* **9**, 149–163 (1992)
- 18.22** K. Theriault: Incoherent multibeam Doppler current profiler performance. Part I: Estimate variance, *IEEE J. Ocean. Eng.* **11**, 7–15 (1986)
- 18.23** T. Chereskin, A. Harding: Modeling the performance of an acoustic Doppler current profiler, *J. Atmos. Ocean. Technol.* **10**, 41–63 (1993)
- 18.24** B. King, E. Cooper: Comparison of ship's heading determined from an array of GPS antennas with heading from conventional gyrocompass measurements, *Deep Sea Res.* **40**, 2207–2216 (1993)
- 18.25** G. Griffiths: Using 3D GPS heading for improving underway ADCP data, *J. Atmos. Ocean. Technol.* **11**, 1135–1143 (1994)
- 18.26** T. Chereskin, C. Harris: *Shipboard Acoustic Doppler Current Profiling During the WOCE Indian Ocean Expedition: I10 , S10-97-14* (Scripps Institution of Oceanography, La Jolla 1997)
- 18.27** T. Chereskin, D. Wilson, L. Beal: The Ekman temperature and salt fluxes at 8°30' N in the Arabian Sea during the 1995 southwest monsoon, *Deep-Sea Res.* **49**, 1211–1230 (2002)
- 18.28** C. Flagg, S. Smith: On the use of the acoustic Doppler current profiler to measure zooplankton abundance, *Deep-Sea Res.* **36**, 455–474 (1989)
- 18.29** A. Gargett: Velcro measurement of turbulence kinetic energy dissipation rate ε , *J. Atmos. Ocean. Technol.* **16**, 1973–1993 (1999)
- 18.30** M. Stacey, S. Monismith, J. Burau: Measurements of Reynolds stress profiles in unstratified tidal flow, *J. Geophys. Res.* **104:10**, 933–949 (1999)
- 18.31** L. Regier: Mesoscale current fields observed with a shipboard profiling acoustic current meter, *J. Phys. Oceanogr.* **12**, 880–886 (1982)
- 18.32** T. Joyce, D. Bitterman, K. Prada: Shipboard acoustic profiling of upper ocean currents, *Deep-Sea Res.* **29**, 903–913 (1982)
- 18.33** E. Firing, R. Gordon: *Deep ocean acoustic Doppler current profiling, Proc. IEEE Fourth International Working Conference on Current Measurements , Clinton, MD* (Ocean Engineering Society, Arlington 1990)
- 18.34** J. Fischer, M. Visbeck: Deep velocity profiling with self-contained ADCPs, *J. Atmos. Ocean. Technol.* **10**, 764–773 (1993)
- 18.35** W. Munk, P. Worcester, C. Wunsch: *Ocean Acoustic Tomography* (Cambridge Univ Press, Cambridge 1995)
- 18.36** http://www.nodc.noaa.gov/OC5/WOA05/pr_woa05.html
- 18.37** W. Munk, C. Wunsch: Abyssal recipes II: Energetics of tidal and wind mixing, *Deep-Sea Res.* **26**, 123–161 (1979)
- 18.38** W. Munk, C. Wunsch: Observing the ocean in the 1990s, *Phil. Trans. R. Soc. London* **307**, 439–464 (1982)
- 18.39** B. Dushaw, G. Bold, C.-S. Chiu, J. Colosi, B. Cornuelle, Y. Desaubies, M. Dzieciuch, A. Forbes, F. Gaillard, J. Gould, B. Howe, M. Lawrence,

- J. Lynch, D. Menemenlis, J. Mercer, P. Mikhalevsky, W. Munk, I. Nakano, F. Schott, U. Send, R. Spindel, T. Terre, P. Worcester, C. Wunsch: *Observing the ocean in the 2000's: A strategy for the role of acoustic tomography in ocean climate observation, Observing the Oceans in the 21st Century*, C. Koblinsky and N. Smith (GODAE Project Office and Bureau of Meteorology, Melbourne 2001)
- 18.40** B. Dushaw, G. Egbert, P. Worcester, B. Cornuelle, B. Howe, K. Metzger: A TOPEX/POSEIDON global tidal model (TPXO.2) and barotropic tidal currents determined from long-range acoustic transmissions, *Prog. Oceanogr.* **40**, 337–367 (1997)
- 18.41** The AMODET Group (T. Birdsall, J. Boyd and B. Cornuelle B. and Howe and R. Knox and J. Mercer and K. Metzger and R. Spindel and P. Worcester): Moving ship tomography in the northwest Atlantic Ocean, *EOS Trans. AGU* **75**, 17–23 (1994)
- 18.42** D. Watts, H. Rossby: Measuring dynamic heights with inverted echo sounders: Results from MODE, *J. Phys. Oceanogr.* **7**, 345–358 (1977)
- 18.43** S. Garzoli, A. Bianchi: Time-space variability of the local dynamics of the Malvinas–Brazil confluence as revealed by inverted echo sounders, *J. Geophys. Res.* **92**, 1914–1922 (1987)
- 18.44** C. Meinen, D. Watts: Vertical structure and transport on a transect across the North Atlantic Current near 42N: Time series and mean, *J. Geophys. Res.* **105**:**21**, 891–869 (2000)
- 18.45** D. Watts, C. Sun, S. Rintoul: Gravest empirical modes determined from hydrographic observations in the Subantarctic Front, *J. Phys. Oceanogr.* **31**, 2186–2209 (2001)
- 18.46** J. Colosi, T. Birdsall, C. Clark, J. Colosi, B. Cornuelle, D. Costa, B. Dushaw, M. Dzieciuch, A. Forbes, B. Howe, D. Menemenlis, J. Mercer, K. Metzger, W. Munk, R. Spindel, P. Worcester, C. Wunsch: A review of recent results on ocean acoustic wave propagation in random media: Basin scales, *IEEE J. Ocean. Eng.* **24**, 138–155 (1999)
- 18.47** I. Fukumori: A partitioned Kalman filter and smoother, *Mon. Weather Rev.* **130**, 1370–1383 (2002)
- 18.48** D. Di Iorio, A. Gargett: *Sounds in the Sea: From Ocean Acoustics to Acoustical Oceanography*, ed. by H. Medwin (Cambridge Univ Press, Cambridge 2005)
- 18.49** T. Sanford: Motionally induced electric and magnetic fields in the sea, *J. Geophys. Res.* **76**, 3476–3492 (1971)
- 18.50** A. Chave, D. Luther: Low-frequency, motionally-induced electro-magnetic fields in the ocean, Part 1: Theory, *Geophys. J. Res.* **95**, 7185–7200 (1990)
- 18.51** M. Baringer, J. Larsen: Sixteen years of Florida Current transport at 27 N, *Geophys. Res. Lett.* **28**, 3179–3182 (2001)
- 18.52** A. Chave, D. Luther, J. Filloux: Observations of the boundary current system at 26.5 N in the sub-tropical North Atlantic Ocean, *Phys. J. Oceanogr.* **27**, 1827–1848 (1997)
- 18.53** T. Sanford: *Proc. of the IEEE Third Working Conference on Current Measurement, Airlie, VA* (IEEE, New York 1986)
- 18.54** J. Larsen: Transport and heat flux of the Florida Current at 27N derived from cross-stream voltages and profiling data: Theory and observations, *Phil. Trans. Roy. Soc. London* **338**, 169–236 (1992)
- 18.55** R. Nolasco, F. Monteiro Santos, A. Soares, N. Palashin, P. Represas, J. Dias: Measurements of motional induction voltage in the Ria de Aveiro lagoon (Portugal). In: *Third Int. Workshop of Scientific Use of Submarine Cables and Related Technologies* (IEEE, Piscataway 2003) pp. 127–132
- 18.56** J. Kasahara: *Proc. Scientific Submarine Cable 2003 Workshop*, ed. by A. Chave (University of Tokyo, Tokyo 2003), IEEE, Piscataway, NJ, 2003
- 18.57** T. Sanford, R. Drever, J. Dunlap, W. Johns: *Proc. of the IEEE Fifth Working Conference on Current Measurement*, ed. by S. Anderson, G. Appell, A. Williams (William S. Sullwold, Taunton 1995)
- 18.58** D. Crombie: Proposal for a new Δ ether drift experiment, *Nature* **175**, 681–682 (1955)
- 18.59** D.E. Barrick: *HF Radio Oceanography—Arevier, Boundary-Layer Meteorology* (Springer, Berlin 1978), Historical Archive 4,1–4
- 18.60** C. Teague, J. Vesecky, D. Fernandez: Hf radar instruments, past to present, *Oceanography* **10**, 40–44 (1997)
- 18.61** High frequency radars for coastal oceanography, *Oceanography* **10**(2) (1997)
- 18.62** D. Luther, A. Chave: *Observing integrating variables in the ocean*, Proc. 7th 'Aha Huliko'a Hawaiian Winter Workshop on Statistical Methods in Physical Oceanography (University of Hawaii, Honolulu 2003)
- 18.63** D. Watts, X. Qian, K. Tracey: Mapping abyssal current and pressure fields under the meandering Gulf Stream, *J. Atmos. Ocean. Technol.* **18**, 1052–1067 (2001)
- 18.64** C. Hughes, M. Smithson: Bottom pressure correlations in the south Atlantic, *Geophys. Res. Lett.* **23**, 2243–2246 (1996)
- 18.65** D. Luther, A. Chave, J. Filloux, P. Spain: Evidence for local and nonlocal barotropic responses to atmospheric forcing during BEMPEX, *Geophys. Res. Lett.* **17**, 949–952 (1990)
- 18.66** M. Alford, M. Gregg, M. Merrifield: Structure, propagation and mixing of energetic baroclinic tides in Mamala Bay, Oahu, Hawaii, *J. Phys. Oceanogr.* **36**, 997–1018 (2006)
- 18.67** H. Yamamoto, T. Hatayama, Y. Yoshikawa, M. Fukasawa: The first science deployment of a McLane Moored Profiler, *JAMSTECR* **47**, 1–11 (2003)
- 18.68** E.D. Asaro: Performance of autonomous Lagrangian floats, *Atmos. J. Ocean. Technol.* **20**, 896–911 (2003)

- 18.69 C. Eriksen, T. Osse, R. Light, T. Wen, T. Lehman, P. Sabin, J. Ballard, A. Chiodi: Seaglider: A long-range autonomous underwater vehicle for oceanographic research, *IEEE J. Ocean. Eng.* **26**, 424–436 (2001)
- 18.70 D. Rudnick, T. Boyd, R. Brainard, G. Carter, G. Egbert, M. Gregg, P. Holloway, J. Klymak, E. Kunze, C. Lee, M. Levine, D. Luther, J. Martin, M. Merrifield, J. Moum, J. Nash, R. Pinkel, L. Rainville, T. Sanford: From tides to mixing along the Hawaiian Ridge, *Science* **301**, 355–357 (2003)
- 18.71 A. Jessup: The FAIRS Experiment, *IEEE Geosci. Rem. Sens. Soc. Newsletter* **123**, 12–16 (2002)
- 18.72 M. Aziz, S. Reising, W. Asher, L. Rose, P. Gaiser, K. Horgan: Effects of air-sea interaction parameters on ocean surface microwave emission at 10 and 37 Ghz, *IEEE Trans. Geosci. Remote Sens.* **43**, 1763–1774 (2005)
- 18.73 W. Asher, A. Jessup, M. Atmane: Oceanic application of the active controlled flux technique for measuring air-sea transfer velocities of heat and gases, *J. Geophys. Res.* **109**, C08S12 (2004), DOI: 10.1029/2003JC001862
- 18.74 E. Hintsa, W. Dacey, W. McGillis, J. Edson, C. Zappa, H. Zeelink: Sea-to-air fluxes from measurements of the atmospheric gradient of dimethylsulfide and comparison with simultaneous relaxed eddy accumulation measurements, *J. Geophys. Res.* **109**, C01026 (2004), DOI: 10.1029/2002JC001617
- 18.75 J. Gemmrich, D. Farmer: Near-surface turbulence in the presence of breaking waves,, *J. Phys. Oceanogr.* **34**, 1067–1086 (2004)